Targeting G-quadruplex DNA as cognitive function therapy for ATR-X syndrome

AUTHOR(S):

Shioda, Norifumi; Yabuki, Yasushi; Yamaguchi, Kouya; Onozato, Misaki; Li, Yue; Kurosawa, Kenji; Tanabe, Hideyuki; ... Sugiyama, Hiroshi; Wada, Takahito; Fukunaga, Kohji

CITATION:

Shioda, Norifumi ...[et al]. Targeting G-quadruplex DNA as cognitive function therapy for ATR-X syndrome. Nature Medicine 2018, 24(6): 802-813

ISSUE DATE:

2018-05-21

URL:

http://hdl.handle.net/2433/232509

Targeting G-quadruplex DNA as cognitive function therapy for ATR-X syndrome

Norifumi Shioda[1*], Yasushi Yabuki[2], Kouya Yamaguchi[2], Misaki Onozato[2], Yue Li[3], Kenji Kurosawa[4], Hideyuki Tanabe[5], Nobuhiko Okamoto[6], Takumi Era[7], Hiroshi Sugiyama[3], Takahito Wada[8*] and Kohji Fukunaga[2*]

[1.] Department of Biofunctional Analysis Laboratory of Molecular Biology, Gifu Pharmaceutical University, Gifu, Japan.
[2.] Department of Pharmacology, Graduate School of Pharmaceutical Sciences, Tohoku University, Sendai, Japan.
[3.] Department of Chemistry, Graduate School of Science, Kyoto University, Kyoto, Japan.
[4.] Division of Genetics, Kanagawa Children's Medical Center, Yokohama, Japan.
[5.] Department of Evolutionary Studies of Biosystems, School of Advanced Sciences, SOKENDAI (The Graduate University for Advanced Studies), Hayama, Kanagawa, Japan.
[6.] Department of Medical Genetics, Osaka Women's and Children's Hospital, Osaka, Japan.
[7.] Department of Cell Modulation, Institute of Molecular Embryology and Genetics, Kumamoto University, Kumamoto, Japan.
[8.] Department of Medical Ethics and Medical Genetics, Graduate School of Medicine, Kyoto University, Kyoto, Japan.

Corresponding Authors: Norifumi Shioda, Takahito Wada or Kohji Fukunaga
Department of Biofunctional Analysis Laboratory of Molecular Biology, Gifu Pharmaceutical University, 1-25-4 daigaku-nishi, Gifu 501-1196, Japan (N.S.).
Department of Medical Ethics and Medical Genetics, Kyoto University School of Public Health, Yoshidakonoemachi, Sakyo-ku Kyoto, 606-8501, Japan (T.W.).
Department of Pharmacology, Graduate School of Pharmaceutical Sciences, Tohoku University, 6-3 Aramaki-Aoba, Aoba-ku, Sendai, Miyagi 980-8578, Japan (K.F.).

Email: shioda@gifu-pu.ac.jp (N.S.), wadataka@kuhp.kyoto-u.ac.jp (T.W.) or kfukunaga@m.tohoku.ac.jp (K.F.)

Tel: +81-58-230-8100, **Fax**: +81-58-230-8105 (N.S.)
Tel: +81-75-753-4648, **Fax**: +81-75-753-4649 (T.W.)

Tel: +81-22-795-6836, **Fax**: +81-22-795-6835 (K.F.)

Abstract

Alpha-thalassemia X-linked intellectual disability (ATR-X) syndrome is caused by mutations in *ATRX*, which encodes a chromatin-remodeling protein. Genome-wide analyses in mouse and human cells indicate that ATRX tends to bind G-rich sequences with high potential to form G-quadruplexes. Here, we report that *Atrx* mutation induces aberrant upregulation of Xlr3b expression in mouse brain, an outcome associated with neuronal pathogenesis displayed by ATR-X model mice. We show that ATRX normally binds to G-quadruplexes in CpG islands of the imprinted *Xlr3b* gene, regulating its expression by recruiting DNA methyltransferases. Xlr3b binds dendritic mRNAs, and its overexpression inhibits dendritic transport of CaMKIIα mRNA, promoting synaptic dysfunction. Notably, treatment with 5-ALA, which is converted into G-quadruplex-binding metabolites, reduces RNA polymerase II recruitment and represses *Xlr3b* transcription in ATR-X model mice. 5-ALA treatment also rescues decreased synaptic plasticity and cognitive deficits seen in ATR-X model mice. Our findings suggest a potential therapeutic strategy to target G-quadruplexes and decrease cognitive impairment associated with ATR-X syndrome.

Introduction

ATR-X syndrome (OMIM Entry #301040) a severe intellectual disability, is caused by *ATRX* mutations [1-3]. *ATRX* encodes the switch/sucrose nonfermentable (SWI/SNF)-like chromatin remodeling protein ATRX, which contains two signature motifs. One is a plant homeodomain (PHD) designated the ATRX-DNMT3-DNMT3L (ADD) domain, which binds histone H3 tails, specifically at H3K4me0K9me2/3 [4-6]. The other includes seven helicase subdomains that confer ATPase activity [7, 8].

Genome-wide analysis combining chromatin immunoprecipitation with next-generation sequencing (ChIP-seq) in both primary human erythroid cells and mouse embryonic stem cells (ESCs) shows ATRX enrichment at G-rich variable number tandem repeats (VNTRs), some of which form non-B DNA structures, including G-quadruplexes [9]. ATRX functions as a part of a histone chaperone complex that deposits the histone variant H3.3 onto pericentromeric heterochromatin and telomeres collaborating with death domain-associated protein (DAXX) in HeLa cells [10] and murine ESCs [11, 12]. ATRX/H3.3 co-localization also occurs on the DNA-methylated allele of many imprinted genes and is associated with differentially methylated regions (DMRs) in mouse ESCs [13]. Some imprinted genes show upregulated expression in forebrain of *Atrx* conditional knockout (cKO) mice [14, 15], suggesting that ATRX silences the active allele. Moreover, expression of the autism-related gene *Nlgn4* significantly decreases in forebrain of *Atrx* cKO mice [16]. Imprinting loss in neurons leads to various mental retardation syndromes, including Prader-Willi and Angelman syndromes [17]. However, the relationship between abnormal expression and cognitive dysfunction in ATR-X syndrome remains unclear.

Results

ATRX regulates *Xlr3b* expression in mouse brain

Atrx$^{\Delta E2}$ mice, which are engineered to lack *Atrx* exon 2, show cognitive defects, among other phenotypes [18], and express a mutant protein that corresponds to a variant with an Arg37Stop (R37X) mutation in exon 2 seen in human ATR-X syndrome [19-21]. Moreover, Atrx$^{\Delta E2}$ mice show 80% reduction in ATRX protein levels [18, 19], similar to outcomes seen in 27 individuals with ATR-X syndrome [8]. We employed DNA microarrays to assess transcriptional profiles at post-natal day (P) 90 in hippocampus of wild-type (WT) and Atrx$^{\Delta E2}$ mice. To identify differentially-expressed genes, we used an algorithm combining false discovery rate (FDR) and fold-change in expression, and identified 31 genes (8 upregulated and 23 downregulated) in WT versus Atrx$^{\Delta E2}$ samples. Among them was *Atrx* itself, which was downregulated in Atrx$^{\Delta E2}$ mice (**Supplementary Table 1** for list of genes with an FDR < 0.05 and a log2 fold-change of > 0.5 or < −0.5). Among genes markedly upregulated in Atrx$^{\Delta E2}$ mice were a member of the lymphocyte regulated (Xlr) gene family, *Xlr3a* and the imprinted gene *Xlr3b* [22-24] (**Fig. 1a**, FDR < 0.05 and log2 fold-change of > 0.5). *Xlr3a* and *Xlr3b* genes show 94% protein similarity, and DNA microarrays are limited in their ability to distinguish related factors. Thus, we carried out reverse transcription-PCR (RT-PCR) analysis with a common forward primer and subtype-specific reverse primers (**Supplementary Fig. 1a**). Primer efficiency was confirmed by amplifying respective cDNAs (**Supplementary Fig. 1b**), and distinct *Xlr3a* and *Xlr3b* amplicons were detected on gels (**Supplementary Fig. 1c**, lanes 1 and 2). Then, using these primers, we detected Xlr3b, but not Xlr3a mRNA, in prefrontal cortex, hippocampus, hypothalamus and cerebellum of WT and Atrx$^{\Delta E2}$ mice (**Supplementary Fig. 1c**). Interestingly, quantitative RT-PCR (RT-qPCR) indicated *Xlr3b* transcript upregulation in some brain areas, including hippocampus, of Atrx$^{\Delta E2}$ mice, but not in peripheral tissues (**Fig. 1b**).

Next, in order to investigate changes in Xlr3 protein expression, we generated an Xlr3 antibody. To confirm its specificity, we performed Xlr3 knockout (KO)-validation using Clustered Regularly Interspaced Short Palindromic Repeats (CRISPR)/Cas9 in cultured hippocampal neurons. To do so, we transduced cultured hippocampal neurons with lentivirus harboring U6gRNA-Cas9-2A-GFP plus guide Xlr3 sgRNA (Xlr3-Cas9-GFP) or control lentivirus expressing GFP. Microscopy analysis revealed loss of Xlr3 immunoreactivity in MAP2-positive neurons infected with Xlr3-Cas9-GFP but not control GFP virus (**Supplementary Fig. 1d**). We also confirmed Xlr3b KO efficacy by RT-qPCR in cultured hippocampal neurons (**Supplementary Fig. 1e**).

Western blot analysis with the Xlr3 antibody also showed significantly decreased protein expression in KO relative to WT cultured hippocampal neurons (**Supplementary Fig. 1f**), confirming antibody specificity. Next, we used the Xlr3 antibody to examine Xlr3 protein expression in $Atrx^{\Delta E2}$ mouse prefrontal cortex, hippocampus, hypothalamus and cerebellum tissues by western blot, and observed significant increases in Xlr3 protein levels in brain of $Atrx^{\Delta E2}$ relative to WT mice (**Fig. 1c**).

CpG island (CGI) methylation by DNA methyltransferases (DMNTs) generally represses transcription [25], and cKO mice lacking *Dnmt1* or both *Dnmt1* and *Dnmt3a* in forebrain neurons show increased *Xlr3b* expression [26, 27]. Although ATRX lacks a canonical DNA methyltransferase motif, human *ATRX* mutations are associated with altered DNA methylation patterns at various genomic loci [28]. Moreover, *Xlr3* gene CGIs display similar sequences, and a sequence potentially forming a G-quadruplex structure is specific to *Xlr3b* (**Supplementary Fig. 2a**). Thus, we asked whether ATRX recruits DNMTs to methylate *Xlr3b* CGIs. To do so, we employed bisulfite sequencing to compare DNA methylation levels in *Xlr3b* CGIs of whole brain samples from WT or $Atrx^{\Delta E2}$ mice. Relative to WT mice, $Atrx^{\Delta E2}$ mice showed significantly decreased DNA methylation at *Xlr3b* CGIs, while we observed no difference in DNA methylation levels in CGIs of other Xlr3 subfamily genes between genotypes (**Fig. 1d, Supplementary Fig. 2b**). Circular dichroism (CD) spectra of a synthetic oligodeoxynucleotide containing sequences potentially forming a G-quadruplex in *Xlr3b* CGIs (Xlr3b-ODN) showed a spectrum characteristic of parallel G-quadruplexes in 10 and 100 mM KCl, with maximum absorbance at 265 nm and minimum at 240 nm (**Supplementary Fig. 3a**). This conformational change in physiological conditions (100 mM KCl) was reflected by decreased DNA mobility in gel shift assays performed using native polyacrylamide gel electrophoresis (PAGE) gels (**Supplementary Fig. 3b**). We then undertook dimethyl sulphate (DMS) footprinting of Xlr3b-ODN to assess formation of an intramolecular parallel G-quadruplex consisting of a core of three stacked G-quartets and three loops (**Fig. 1e, Supplementary Fig. 3c**). This analysis confirmed that *Xlr3b* CGI sequences can form parallel G-quadruplex structures.

To assess how ATRX regulates *Xlr3b*, we performed luciferase reporter assays. To do so, we first cloned three different *Xlr3b* genomic sequences into a pGL3 luciferase reporter vector. They included: a 2.0 kb fragment (designated pGL3-2K) upstream of the *Xlr3b* ATG initiation codon; a pGL3-2K deletion mutant lacking G-quadruplex-forming sequences (pGL3-2KΔG4); and a 1 kb *Xlr3b* upstream sequence (pGL3-1KΔCGI) that lacks CGIs. Mouse neuroblastoma Neuro-2a cells transfected

with pGL3-2K showed significantly reduced luciferase activity when co-transfected with ATRX; conversely, luciferase activity relative to controls increased in cells co-transfected with ATRX shRNA (**Fig. 1f**). However, cells transfected with either pGL3-2KΔG4 or pGL3-1KΔCGI showed activity comparable to cells co-transfected with ATRX or ATRX shRNA, suggesting that ATRX regulates *Xlr3b* through the G-quadruplex structure (**Fig. 1f**). We confirmed ATRX shRNA knockdown efficacy by immunoblotting for endogenous ATRX protein in Neuro-2a cells (**Supplementary Fig 4a**). Moreover, Neuro-2a cells co-transfected with pGL3-2K plus DNMTs (DNMT1 or DNMT3A) showed significantly decreased reporter activity relative to respective controls (**Fig. 1g**). However, cells co-transfected with pGL3-2K plus DAXX or H3.3 showed comparable reporter activity. Importantly, cells co-transfected with pGL3-2KΔG4 plus DNMTs showed no change in reporter activity relative to pGL3-2KΔG4 alone. Finally, we methylated pGL3-2K, pGL3-2KΔG4 and pGL3-1KΔCGI constructs using CpG DNA methyltransferase *M.SssI* and assessed the luciferase activity. We observed decreased luciferase activity in methylated pGL3-2K and pGL3-2KΔG4, not in methylated pGL3-1KΔCGI, supporting the idea that CGI methylation inhibits *Xlr3b* expression (**Fig. 1g**).

To determine whether ATRX and interacting factors target *Xlr3b* CGIs in mouse hippocampus, we performed ChIP-qPCR with an ATRX antibody. We confirmed that hippocampal samples from $Atrx^{\Delta E2}$ mice contained detectable levels of ATRX protein: those lysates showed an 80% reduction in ATRX protein levels relative to lysates from WT mice, and the ATRX antibody recognized both WT and mutant ATRX protein as described in [18, 19] (**Supplementary Fig. 4b**). Co-immunoprecipitation in hippocampal lysates revealed that ATRX interacts with DNMT1, DNMT3A, DAXX and H3.3 from both WT and $Atrx^{\Delta E2}$ mice, and relatively low amounts of DNMT1, DNMT3A, H3.3 and DAXX were detected in immunoprecipitated samples of $Atrx^{\Delta E2}$ mice (**Supplementary Fig. 4c**). We detected substantial ATRX enrichment at *Xlr3b* CGIs containing G-quadruplexes based on ChIP analysis with primers targeting *Xlr3b* region R1 in chromatin isolated from WT mouse hippocampus, while ATRX interaction with chromatin at this site was greatly decreased in $Atrx^{\Delta E2}$ hippocampus (**Fig. 1h**). Levels of DNMT1, DNMT3A, DAXX and H3.3 also significantly decreased in $Atrx^{\Delta E2}$ relative to WT chromatin in the R1 region. Also, quantitative profiling of ATRX, DNMTs, DAXX and H3.3 across an unrelated R2 region revealed small peaks, demonstrating enrichment of these proteins at *Xlr3b* CGIs (**Fig. 1h**). These observations suggest overall that ATRX binds to parallel G-quadruplexes in *Xlr3b* CGIs along with DNMTs, DAXX and H3.3, where it regulates *Xlr3b* gene expression.

Neuronal RNA granules contain Xlr3b

We next undertook a proteomic screen to search for Xlr3 interaction partners by performing liquid chromatography-tandem mass spectrometry (LC-MS/MS) of proteins pulled down from lysates of P60 WT mouse brain with an Xlr3 antibody. LC-MS/MS analysis revealed an endogenous Xlr3 complex containing multiple components, including actin/myosin-related proteins, dynein motor complex (DYNLL, DYNLRB, DYNLT and DYNC1LI2) proteins, ribonucleoproteins (hnRNP A/B and hnRNP D), 40S ribosomal proteins (RPS10 and RPS25), and others (**Fig. 2a, Supplementary Table 2**). We then confirmed association of purified GST-Xlr3b protein with hnRNP A/B, hnRNP D, DYNLL and DYNC1LI2 by *in vitro* pull-down assays in mouse hippocampal lysates (**Fig. 2b**). Purified Xlr3b protein did not bind F-actin, and its presence did not alter actin polymerization (**Supplementary Fig. 5a, 5b**). To confirm interactions *in vivo*, we performed immunoprecipitation of mouse hippocampal extracts with an Xlr3 antibody followed by immunoblotting with hnRNP A/B, hnRNP D, DYNLL, or DYNC1LI2 antibodies and observed co-precipitation of all with Xlr3 (**Fig. 2c**).

To determine Xlr3 cellular localization, we undertook immunofluorescence of mature MAP2-positive cultured neurons with an Xlr3 antibody. Xlr3 was localized to nuclei and perinuclear areas and seen in granules in MAP2-positive dendrites and in synaptic synaptophysin-positive puncta (**Fig. 2d**). Xlr3-positive structures of this type were also observed in MAP2-positive dendrites in mouse hippocampal CA1 analyzed at P60 (**Fig. 2e**). In dendrites, Xlr3-positive puncta co-localized with hnRNP A/B and cytotoxic granule-associated RNA binding protein 1 (TIA1), both found in RNA granules [29], and with SYTO14-visualized RNA. Xlr3-positive granules did not co-localize with DCP1a, a marker of RNA-processing bodies [29] (**Fig. 2f**).

Xlr3b exhibits a predicted nuclear localization signal (NLS) at amino acid (AA) residues 2-11; residues 74-200 also constitute a conserved Cor1/Xlr/Xmr region (Cor1 domain). To assess function of those sequences, we transfected Neuro-2a cells with FLAG-tagged Xlr3b or similarly-tagged deletion mutants shown in Figure 2g and analyzed their location by confocal microscopy (**Fig. 2g**). Based on FLAG expression, full length (FL)-Xlr3b significantly co-localized with TIA1 in nuclear regions compared to that of non-transfected cells. FL-Xlr3b also accumulated with hnRNP A/B in nuclei, but not with DCP1a (**Fig. 2g**, **Supplementary Fig. 6a, 6b**). Cells transfected with constructs lacking AA 2-11 (ΔNLS) or 74-123 (Δ74-123) showed partial loss of Xlr3b nuclear localization, but localization of the interacting proteins TIA1 and hnRNP A/B

was unchanged. These localization patterns were similar to those seen in FL-Xlr3b-transfected cells (**Fig. 2g**, **Supplementary Fig. 6a, 6b**). Deletion of AA 124-200 (Δ124-200) caused loss of nuclear Xlr3b expression and localization of tagged protein in cytoplasmic ubiquitin-positive inclusion-like structures, in which DCP1a, TIA1 and hnRNP A/B were also colocalized. In addition, the Δ158-170 mutant was distributed similarly to the Δ124-200 mutant (**Fig. 2g**, **Supplementary Fig. 6a, 6b and 6c**). Importantly, nuclear localization of TIA1 and hnRNP A/B in cells transfected with Δ124-200 or Δ158-170 constructs was very similar to patterns observed in non-transfected cells (**Fig. 2g**, **Supplementary Fig. 6a**).

To confirm interactions of Xlr3b AA 158-170 with RNA binding proteins (RBPs), we used Xlr3b inhibitory peptide (XIP), a 29-AA peptide containing Xlr3b AA 158-170 plus the cell-permeable antennapedia homeodomain (ANTP) peptide (**Supplementary Fig. 7a**). When FL-Xlr3b-transfected cells were treated with XIP (1μM for 4 h), TIA1 did not accumulate in the nucleus (**Supplementary Fig. 7b**). We confirmed that XIP, but not the ANTP control peptide, bound to RBPs, TIA1 and hnRNP A/B using pull-down assays of mouse hippocampal lysates with an ANTP antibody (**Supplementary Fig. 7c**). Immunoprecipitation confirmed that FLAG-tagged FL, Δ74-123, Δ124-200 and Δ158-170 mutants were immunoprecipitated with a FLAG antibody. Immunoblotting with TIA1 and hnRNP A/B antibodies detected immunoreactive TIA1 and hnRNP A/B bands in samples transfected with FL and Δ74-123, but not in Δ124-200 and Δ158-170. Remarkably, interactions with TIA1 and hnRNP A/B were not seen in FL-Xlr3b-transfected cells treated with 1μM XIP for 4 h before immunoprecipitation (**Fig. 2h**), suggesting that Xlr3b residues 158-170 are critical for RBP binding. Ubiquitination of Xlr3b Δ124-200 and Δ158-170 may prevent binding to RBPs, regardless of co-localization [30]. Thus, to assess potential Δ124-200 and Δ158-170 ubiquitination, we performed immunoprecipitation of lysates of cells transfected with FLAG-tagged FL, Δ74-123, Δ124-200 and Δ158-170 mutants with a FLAG antibody followed by immunoblotting with a ubiquitin antibody. We confirmed ubiquitination in immunoprecipitants of constructs Δ124-200 and Δ158-170, but ubiquitination was little seen in FL or Δ74-123 proteins (**Supplementary Fig. 6d**).

Phylogenetic analysis identified the FAM9 gene family as human Xlr orthologues, and FAM9 proteins are predicted to have a Cor1 domain [32]. BLAST searches indicated that Xlr3b residues 158-170 are highly conserved in Cor1 domains of FAM9 family proteins, including FAM9A and FAM9B (**Supplementary Fig. 6e**). We observed nuclear localization of FLAG-tagged FAM9A overexpressed in Neuro-2a cells, while a similar construct lacking residues analogous to Xlr3b 158-170 was found in

cytoplasmic inclusion body-like structures in a pattern similar to Xlr3b Δ158-170 transfected cells (**Supplementary Fig. 6e**).

Aberrant Xlr3b expression in neurons decreases synaptic plasticity by inhibiting transport of dendritic CaMKIIα mRNA

In neurons, RNA granules are rapidly transported to dendrites, a process regulated by motor proteins [32]. Some RBPs including hnRNP A/B recognize a specific *cis*-acting element termed the hnRNP A2 response element (A2RE) in mRNA 3' untranslated regions (3' UTRs); these include Ca^{2+}/calmodulin-dependent protein kinase IIα (CaMKIIα), activity-regulated cytoskeleton-associated protein (Arc) and brain-derived neurotrophic factor (BDNF) [33]. Because Xlr3b interacts with the dynein motor complex and RBPs, we hypothesized that Xlr3b regulates dendritic mRNA transport via a dynein-mediated transport mechanism.

To test this hypothesis, we undertook RNA immunoprecipitation in mouse hippocampal lysates to determine whether an endogenous Xlr3 complex associates with dendritic mRNAs. After immunoprecipitation with an Xlr3 antibody, we isolated total RNA from precipitates and analyzed it by qPCR with primers specific to CaMKIIα, Arc and BDNF mRNA 3' UTRs. Immunoprecipitates contained all three mRNAs, and XIP treatment (1μM for 2h) of cell lysates significantly blocked these interactions (**Fig. 3a**).

$Atrx^{\Delta E2}$ mice show cognitive impairment and CaMKIIα dysfunction [18, 19]. Thus we focused on dendritic CaMKIIα mRNA. To determine whether Xlr3b protein is co-transported into dendrites with CaMKIIα mRNA, we used dual-color time-lapse imaging with mCherry-Xlr3b and GFP-MS2-labeled CaMKIIα mRNA (GFP-CaMKIIα 3′ UTR) [34]. mCherry-Xlr3b co-localized with the GFP-CaMKIIα 3′ UTR, and both were co-transported to dendrites of cultured neurons (**Fig. 3b**). By contrast, co-localization of mCherry-Xlr3b mutants (Δ124-200 and Δ158-170) with GFP-CaMKIIα 3′ UTR immunofluorescence was rarely seen (**Supplementary Fig. 8a**). To analyze dynamics of dendritic CaMKIIα mRNA transport, we investigated movement of the GFP-CaMKIIα 3′ UTR in proximal dendrites (20-100μm away from the cell body). Granules moved in anterograde (white arrowhead) and retrograde (yellow arrowhead) directions (**Fig. 3c, top panel, left**). **Fig. 3c** (top panel, right) shows a representative kymograph corresponding to 15-min of live imaging generated from a proximal dendrite that GFP-CaMKIIα 3' UTR (**also see Supplementary Video 1**). Imaging of GFP-CaMKIIα 3′ UTR movement revealed that approximately half of the observed CaMKIIα mRNA granules were immobile, and the few mobile granules showed bidirectional movement in cultured WT neurons. The number of bidirectionally-mobile

CaMKIIα mRNA granules significantly decreased in cultured neurons of transgenic mice overexpressing Xlr3b driven by the neuron-specific Thy1.2 promoter (Thy1-Xlr3b TG mice; **Supplementary Fig. 9a-9d**), relative to effects seen in WT neurons. Moreover, in cultured neurons of Atrx$^{\Delta E2}$ mice, the number of bidirectionally-mobile CaMKIIα mRNA granules significantly decreased. Xlr3b-shRNA transfection or XIP treatment antagonized decreases in dendritic CaMKIIα mRNA transport seen in Atrx$^{\Delta E2}$ neurons, suggesting that Xlr3b acting through RBPs inhibits CaMKIIα mRNA transport (**Fig. 3c, bottom**). We confirmed efficacy of Xlr3b knockdown by immunoblotting of endogenous Xlr3 protein in cultured neurons (**Supplementary Fig 9e**). In addition, dynamics of CaMKIIα mRNA transport in distal dendrites (100-200μm from the cell body) was similar to that seen in proximal dendrites: bidirectionally-mobile CaMKIIα mRNA granules significantly decreased in Thy1-Xlr3b TG and Atrx$^{\Delta E2}$ neurons relative to effects seen in WT neurons. Furthermore, Xlr3b-shRNA transfection or XIP treatment rescued decreases in dendritic CaMKIIα mRNA transport seen in Atrx$^{\Delta E2}$ neurons (**Supplementary Fig. 8b, Supplementary Video 2**).

RNA granules localize beneath postsynaptic sites in dendrites, and CaMKIIα mRNA is located in dendrites and active postsynaptic regions [33]. Indeed, the number of double-positive protein puncta containing the GFP-CaMKIIα 3′ UTR and the postsynaptic marker PSD95 significantly decreased in cultured neurons of Thy1-Xlr3b TG and Atrx$^{\Delta E2}$ mice relative to the number seen in WT mice, and cultured neurons from Atrx$^{\Delta E2}$ mice transfected with Xlr3b shRNA or treated with XIP showed a significant increase in the number of double-positive puncta (**Fig. 3d**). Next, we performed western blot analysis for CaMKIIα protein in synaptosomal membrane fractions, containing PSD95 isolated from cultured hippocampal neurons (**Supplementary Fig. 9f**). CaMKIIα protein was decreased in the synaptosomal membrane fractions from cultured neurons of Thy1-Xlr3b TG and Atrx$^{\Delta E2}$ mice relative to that seen in WT mice. XIP treatment in Atrx$^{\Delta E2}$ neurons significantly increased in the synaptosomal CaMKIIα protein levels without changes in both CaMKIIα and PSD95 levels in total cell lysate fractions between groups (**Supplementary Fig. 9f**).

Dendritic CaMKIIα mRNA translation is regulated by synaptic activity, and postsynaptic CaMKIIα protein regulates hippocampal long-term potentiation (LTP), which is critical for learning and memory [35-38]. To assess a potential effect on LTP, we undertook electrophysiological analysis of brain slices from hippocampal CA1. Consistent with our previous study [19], we observed markedly reduced high frequency stimulation (HFS)-induced LTP in Atrx$^{\Delta E2}$ mice, which was significantly rescued by a 2 h bath application of XIP to Atrx$^{\Delta E2}$ mouse samples, but not following application of an

ANTP control peptide, suggesting that impaired LTP seen in Atrx$^{\Delta E2}$ mice is in part Xlr3b-dependent (**Fig. 3e**). Notably, Thy1-Xlr3b TG mice also showed impaired hippocampal LTP (**Supplementary Fig. 9g**). We observed no significant difference in basic electrophysiological properties, among them input-output relations and paired-pulse ratio, between groups (**Supplementary Fig. 9h**). LTP induction, which strengthens synapses, results in CaMKII phosphorylation throughout the dendritic area, suggesting widespread CaMKII activation including in spines [39, 40]. In WT mice, levels of CaMKIIα phosphorylation significantly increased following hippocampal LTP induction. Consistent with LTP impairment, CaMKIIα phosphorylation did not increase following LTP induction in hippocampus of Atrx$^{\Delta E2}$ and Thy1-Xlr3b TG mice. Notably, bath application of XIP, but not ANTP, significantly restored LTP-induced CaMKIIα phosphorylation in the Atrx$^{\Delta E2}$ hippocampus (**Supplementary Fig. 9i**).

To assess whether Xlr3b overexpression affects cognitive function, we employed a novel object recognition task. In training trials, we observed no differences in the discrimination index using the same object between WT and Thy1-Xlr3b TG mice (data not shown). After a 24 h retention interval between trial and test sessions, Thy1-Xlr3b TG mice showed a significantly lower discrimination index for a novel object than did WT mice (**Supplementary Fig. 9j**). To assess contextual memory, we undertook a fear-conditioned passive avoidance task and observed no significant differences in latency to enter a dark room in the absence of foot shock between WT and Thy1-Xlr3b TG mice (data not shown). However, latency to enter the dark compartment was markedly decreased 1-week after foot shock in Thy1-Xlr3b relative to WT mice (**Supplementary Fig. 9k**). We then used a Y-maze to test spatial working memory and observed that Thy1-Xlr3b mice showed impairment based on the percentage of alternation behaviors relative to WT mice without a change in the total number of arm entries (**Supplementary Fig. 9l**).

5-ALA treatment reduces RNA polymerase II recruitment and represses *Xlr3b* transcription by modifying G-quadruplex structure.

G-quadruplex-binding small molecules such as porphyrin function as transcriptional repressors [41]. Thus, we asked whether *Xlr3b* repression via porphyrin binding its G-quadruplex structure would antagonize synaptic dysfunction and cognitive deficits seen in Atrx$^{\Delta E2}$ mice. To do so, we first assessed intracellular generation of porphyrins following administration of 5-aminolevulinic acid (5-ALA), which can be metabolized to porphyrins, protoporphyrin IX (PpIX) and hemin [42] (**Fig. 4a**). We confirmed PpIX and hemin binding to Xlr3b-ODN G-quadruplexes using UV melting

analysis. The ΔT_m for PpIX and hemin was 2.0 and 2.3°C, respectively, indicating that PpIX and hemin both moderately bind *Xlr3b* G-quadruplexes structure. The ΔT_m for TMPyP4, a well-known G-quadruplex binding ligand, was higher than 4°C (**Supplementary Fig. 10a**). To determine whether 5-ALA treatment alters *Xlr3b* gene expression, we transfected Neuro-2a cells with the pGL3-2K reporter, treated cells with varying concentrations of 5-ALA or TMPyP4, and assessed effects of *Xlr3b* expression based on luciferase assays. As expected, treatment with 5-ALA or TMPyP4 reduced luciferase activity dose-dependently but had no effect on cells transfected with pGL3-2KΔG4 (**Fig. 4b, Supplementary Fig. 10b**). Decreased luciferase activity in 5-ALA treated cells was efficiently rescued by co-treatment with the 5-ALA dehydratase inhibitor succinylacetone (**Fig. 4c**). Next, we asked whether treatment with G-quadruplex ligands would inhibit aberrant *Xlr3b* gene expression seen in Atrx$^{\Delta E2}$ mouse brain. To do so, we administered 5-ALA (p.o. daily from P30 to P90) or TMPyP4 (i.p. twice weekly from P30 to P90). Either treatment significantly blocked increases in hippocampal Xlr3b mRNA and Xlr3 protein seen in vehicle-treated Atrx$^{\Delta E2}$ mice (**Fig. 4d and 4e, Supplementary Fig. 10c and 10d**).

To investigate mechanisms underlying these effects, we undertook bisulfite sequencing to compare DNA methylation levels. *Xlr3b* CGIs in hippocampus and prefrontal cortex of Atrx$^{\Delta E2}$ mice showed significantly decreased DNA methylation relative to WT mice, an effect unchanged by 5-ALA treatment (**Fig. 4f, Supplementary Fig. 10e**). Next, we performed ChIP-qPCR of ATRX and RNA polymerase II (Pol II) within the *Xlr3b* gene, as G-quadruplex structures hinder Pol II passage [43, 44]. The prediction of quadruplex structures within the *Xlr3b* gene was supported by the G-quadruplex analysis tool QGRS Mapper [45] (**Fig. 4g, top**). In WT mouse hippocampus, ATRX and Pol II accumulated at *Xlr3b* CGIs containing G-quadruplexes, based on analysis using primers targeting amplicon 1, but little signal was seen at amplicons 2, 3 and 4 (**Fig. 4g, bottom**). However, in Atrx$^{\Delta E2}$ mouse, we detected an elevated Pol II signals across all amplicons in the *Xlr3b* gene body as well as CGIs, indicating enhanced *Xlr3b* transcription. Furthermore, elevated Pol II signals were significantly attenuated following 5-ALA treatment (**Fig. 4g, bottom**). These results suggest that the porphyrin metabolites PpIX and hemin, which are derived from 5-ALA, bind *Xlr3b* G-quadruplex structures, partially reducing Pol II recruitment.

Treatment with G-quadruplex ligands counteracts cognitive deficits seen in Atrx$^{\Delta E2}$ mice.

Next, we asked whether 5-ALA treatment rescued decreases in dendritic CaMKIIα mRNA transport seen in Atrx$^{\Delta E2}$ neurons. Imaging of GFP-CaMKIIα 3′ UTR movement revealed that the decreased number of bidirectionally-mobile CaMKIIα mRNA granules was significantly rescued in 5-ALA treated Atrx$^{\Delta E2}$ neurons (7 days, 1μM) at proximal and distal dendrites (**Fig. 5a, Supplementary Fig. 11a**). The decreased number of double-positive protein puncta containing GFP-CaMKIIα 3′ UTR and PSD95 in Atrx$^{\Delta E2}$ neurons was also significantly rescued (**Fig. 5b**). Moreover, reduced HFS-induced LTP in hippocampus of vehicle-treated Atrx$^{\Delta E2}$ mice was significantly restored in 5-ALA-treated Atrx$^{\Delta E2}$ mice (p.o. daily from P30 to P90) without a change in basic electrophysiological properties (**Fig. 5c, Supplementary Fig. 11b**). Finally, 5-ALA treatment significantly blocked decreased CaMKIIα protein level at synaptosomal membrane fractions in cultured hippocampal neurons from Atrx$^{\Delta E2}$ mice, and restored LTP-induced CaMKIIα phosphorylation in hippocampus of Atrx$^{\Delta E2}$ mice (**Supplementary Fig. 11c**).

We next administered 5-ALA (p.o. daily from P30 to P90) or TMPyP4 (i.p. twice weekly from P30 to P90) to Atrx$^{\Delta E2}$ mice and subsequently assessed memory-related behaviors. We observed no differences in a novel object recognition task in the discrimination index using the same object in all groups in training trials (data not shown). After a 24h retention interval between trial and test sessions, Atrx$^{\Delta E2}$ mice showed a significantly lower discrimination index for a novel object than did WT mice. The discrimination index for the novel object in Atrx$^{\Delta E2}$ mice treated with 5-ALA or TMPyP4 was significantly higher than that seen in vehicle-treated groups (**Fig. 5d, Supplementary Fig. 11d**). In a fear-conditioned passive avoidance task, we observed no significant differences in latency to enter a dark room in the absence of foot shock in all groups (data not shown). However, latency to enter a dark compartment was markedly decreased 1-week after foot shock in Atrx$^{\Delta E2}$ relative to WT mice. 5-ALA or TMPyP4 administration also significantly rescued reduced latency time (**Fig. 5e, Supplementary Fig. 11e**). In a Y-maze test, Atrx$^{\Delta E2}$ mice showed impairment based on the percentage of alternation behaviors relative to WT mice without a change in the total number of arm entries. 5-ALA or TMPyP4 administration significantly increased the percentage of spontaneous alternation behaviors in Atrx$^{\Delta E2}$ mice (**Fig. 5f, Supplementary Fig. 11f**). Many patients with ATR-X syndrome exhibit abnormal social behaviors, especially shyness and social withdrawal [46]. Interestingly, in interactions with WT mice, Atrx$^{\Delta E2}$ mice showed enhanced passivity, greater escape duration and decreased active social behaviors, such as following and sniffing. These changes were dramatically ameliorated in Atrx$^{\Delta E2}$ mice (**Supplementary Fig. 11g**).

Acute administration of a single 5-ALA dose (10mg/kg, p.o.) did not ameliorate impaired learning and memory-related behaviors in Atrx$^{\Delta E2}$ mice (data not shown).

To confirm that TMPyP4 was present in brain, we measured TMPyP4 fluorescence levels, as described in [47]. Chronic intraperitoneal injection of TMPyP4 (i.p. twice weekly from P30 to P90) in mice increased fluorescence levels in some tissues, including brain, suggesting that treatment allows intracerebral transferability and enables TMPyP4 accumulation in brain tissue (**Supplementary Fig. 11h**). However, we stopped chronic TMPyP4 administration on day 60 due to toxicity, as evidenced by reduced body weight (**Supplementary Fig. 11i**). Unlike the case with TMPyP4, 5-ALA pharmacokinetics and biodistribution, including in brain, has been reported in humans [48] and rodents [49]. We confirmed that 5-ALA crosses the blood brain barrier after oral administration. In mouse brain, 5-ALA (3mg/kg, p.o.) levels peaked at 30min and then decreased to basal levels by 24h after administration (**Supplementary Fig. 11j**).

To investigate expression of other genes underlying these effects, we performed DNA microarray analysis of RNA extracted from hippocampus of P90 WT, Atrx$^{\Delta E2}$, or 5-ALA treated Atrx$^{\Delta E2}$ mice, and focused on 31 genes differentially expressed (8 upregulated and 23 downregulated) in WT versus Atrx$^{\Delta E2}$ samples using a threshold of FDR <0.05 and log2 fold-change of > 0.5 or < -0.5 (**Supplementary Table 1**). Rescued or not rescued genes were assessed using the difference between the average value in log2 global normalization. 5-ALA treatment of Atrx$^{\Delta E2}$ mice significantly blocked differential expression of 71.0% of genes including *Xlr3b* (**Fig. 5g, Supplementary Table 3**). Following analysis of mice treated with TMPyP4, we selected 138 genes differentially expressed (38 upregulated and 100 downregulated) in WT versus Atrx$^{\Delta E2}$ hippocampal samples using a threshold of log2 fold-change of > 1.0 or < -1.0. TMPyP4 treatment of Atrx$^{\Delta E2}$ mice blocked differential expression of 92.8% of genes including *Xlr3b,* leaving only 10 of 138 genes remained differentially expressed (**Supplementary Table 4**).

Discussion

Here, we make several critical observations relevant to activities of ATRX (**Supplementary Fig. 12**). (1) ATRX binds to parallel G-quadruplexes in *Xlr3b* CGIs together with DNMTs, DAXX and H3.3, where it regulates *Xlr3b* gene expression. (2) Cognitive deficits seen in $Atrx^{\Delta E2}$ mice are accompanied by Xlr3b upregulation, which inhibits CaMKIIα mRNA transport in neuronal dendrites. (3) Abnormal neuronal phenotypes exhibited by $Atrx^{\Delta E2}$ mice are rescued by treatment with 5-ALA, a G-quadruplex ligand that inhibits Xlr3b expression.

Among genes altered in $Atrx^{\Delta E2}$ mouse brain, the imprinted gene Xlr3b is significantly overexpressed. ATRX is enriched with DNMTs at G-quadruplexes in *Xlr3b* CGIs. We observed that reduced ATRX levels at a given site were accompanied by reduced DNMT levels and substantial DNA demethylation, suggesting that ATRX regulates DNA methylation by DNMT recruitment to G-quadruplexes. Notably, forebrain-specific cKO of either DNMT1 or both DNMT1 and DNMT3A reportedly promotes increased *Xlr3b* expression in excitatory neurons [26, 27]. Moreover, recent genome-wide analysis revealed preferential ATRX localization at the DNA-methylated allele of many imprinted DMRs in mouse ESCs and that ATRX-bound CGI sequences were methylated to a greater extent than that seen in other parts of the genome [13]. ATRX deficiency also correlates with reduced H3.3 incorporation and with Pol II stalling at G-rich intragenic sites, indicating that ATRX influences Pol II-mediated transcription [16]. Accordingly, we detected Pol II accumulation at *Xlr3b* CGIs harboring G-quadruplexes in WT hippocampus. We also found that cells in the $Atrx^{\Delta E2}$ hippocampus showed enriched Pol II signals across the *Xlr3b* gene relative to cells from WT brain, and elevated Pol II signals in $Atrx^{\Delta E2}$ hippocampus were significantly attenuated following 5-ALA treatment without changing DNA methylation levels. These results suggest that the porphyrin metabolites PpIX and hemin, which are derived from 5-ALA, bind G-quadruplex structures, partially inhibiting Pol II recruitment, a mechanism supported by biophysical analysis of G-quadruplexes in the *HIF1A, KRAS, CMYB* and *CMYC* genes [41]. The G-quadruplex structure formed behind advancing Pol II may be recognized by other factors, including positive transcription elongation factor b [50]. In this context, further studies are required to define dynamic transcriptional structures interacting with the region bearing G-quadruplex motifs and how they regulate ATRX-mediated DNA methylation and Pol II recruitment.

We also report a novel role for Xlr3b as a component of RNA granules containing RBPs, which inhibit CaMKIIα mRNA transport into neuronal dendrites. Xlr3b interacted with the dendritic mRNAs CaMKIIα, Arc and BDNF via a 13 AA Cor1

domain, which binds RBPs. This sequence is required for CaMKIIα mRNA transport, suggesting that RBP binding is also necessary for transport. Interestingly, that Xlr3b sequence is highly conserved in human FAM9 proteins, which also exhibit a Cor1 domain. Thus, binding ability may be common to proteins containing Cor1/Xlr/Xmr motifs. In addition, our fluorescence imaging and electrophysiological analysis supports the idea that Xlr3b negatively regulates synaptic plasticity by inhibiting dendritic CaMKIIα mRNA transport in Atrx$^{\Delta E2}$ mice. Mice engineered to lack the CaMKIIα mRNA 3′ UTR showed reduced levels of CaMKIIα transcripts at postsynaptic densities, reduced LTP, and impaired spatial memory [38]. Dendritic transport and local translation of BDNF and Arc mRNA in synapses also enhances neuronal activity [33], strongly suggesting that Xlr3b-mediated dendritic mRNA transport is related to learning and memory functions. 39X^{m}O mice, a murine model of the female developmental disorder Turner syndrome, show aberrantly high *Xlr3b* expression in brain, an outcome associated with difficulties in performing a reversal learning test, relative to 40XX and 39X^{p}O mice [24], suggesting that Xlr3b governs mouse behaviors. However, mechanisms underlying these activities remain unknown. We also demonstrated that Thy1-Xlr3b TG mice show impaired LTP and memory deficits, indicating that aberrant neuronal Xlr3b expression partially affects dendritic mRNA transport and learning behaviors in Atrx$^{\Delta E2}$ mice.

We also show that administration of the G-quadruplex ligands 5-ALA or TMPyP4 significantly rescues neuronal phenotypes seen in Atrx$^{\Delta E2}$ mice by inhibiting Xlr3b transcription. However, recovery of cognitive deficits in Atrx$^{\Delta E2}$ mice following 5-ALA administration may be due in part to the binding of ligand to G-quadruplexes of other ATRX targets, although this activity remains unknown. G-quadruplex motifs broadly influence transcription and translation [41]. In addition, ATRX can either repress or activate gene expression through G-quadruplexes [9, 51, 52]. Although potential off-target effects remain to be investigated, our findings suggest a novel therapeutic strategy aimed at blocking Xlr3b expression through small molecule binding to G-quadruplex DNA in patients with ATR-X syndrome. Among candidate ligands, 5-ALA has been applied clinically with minimal risk and approved for use following intracranial tumor resection in Europe, Canada, and Japan [53], where it has been used as a photosensitizer in photodynamic diagnostics applied in neurosurgery [54]. 5-ALA is also safe when administered chronically up to 200 mg per day in humans [55]. Thus, its approval time would be short and the cost of clinical trials would be reduced, as pre-existing absorption, distribution, metabolism, excretion (ADME) and toxicity data is available. Finally, the risk of failure is reduced as data relevant to 5-ALA safety and

pharmacology is available.

In summary, our study indicates that G-quadruplex ligands regulate gene expression through a transcriptional mechanism involving Xlr3b and could be used to treat symptoms associated with ATR-X syndrome.

Accession codes availability: Microarray raw data are available at Gene Expression Omnibus (GEO); accession numbers, GSE103031 and GSE103032.

Data Availability Statement: Summary of all statistical data was shown in Supplementary Table 5. The other data that support the findings of this study are available from the corresponding authors on reasonable request.

Acknowledgments: We thank D. Picketts for kindly providing ATRX cDNA (pEGFP-C2-ATRX-HA) plasmid, N. Berube for kindly providing ATRX shRNA (pSUPER-shATRX1) plasmid, and K. Kosik for kindly providing GFP-MS2-nls and MS2 binding site (MS2bs)-CaMKIIα 3′UTR plasmids. This research was supported by the Practical Research Project for Rare/Intractable Diseases from the Japan Agency for Medical Research and Development, AMED. (N.S., K.K., H.T., N.O., H.S., K.F. and T.W.). This work was also supported by MEXT/JSPS KAKENHI (Grant Numbers 16K08265 and 25110705) to N.S.

Author contributions: N.S., Y.Y., K.Y., M.O., and Y.L. performed experiments. K.K., H.T., N.O., T.E., H.S. and T.W. provided critical advice. N.S. and K.F. wrote the manuscript and designed the study. All authors discussed the results and commented on the manuscript.

Competing interests: The authors declare no competing financial interests.

References (for main text only)

1. Gibbons RJ, Suthers GK, Wilkie AO, Buckle VJ, Higgs DR. X-linked alpha-thalassemia/mental retardation (ATR-X) syndrome: localization to Xq12-q21.31 by X inactivation and linkage analysis. Am J Hum Genet. 51, 1136-1149. (1992)

2. Gibbons RJ, Picketts DJ, Villard L, Higgs DR. Mutations in a putative global transcriptional regulator cause X-linked mental retardation with alpha-thalassemia (ATR-X syndrome). Cell. 80, 837-845. (1995)

3. Gibbons RJ, Wada T, Fisher CA, Malik N, Mitson MJ, Steensma DP, Fryer A, Goudie DR, Krantz ID, Traeger-Synodinos J. Mutations in the chromatin-associated protein ATRX. Hum Mutat. 29, 796-802. (2008)

4. Argentaro A, Yang JC, Chapman L, Kowalczyk MS, Gibbons RJ, Higgs DR, Neuhaus D, Rhodes D. Structural consequences of disease-causing mutations in the ATRX-DNMT3-DNMT3L (ADD) domain of the chromatin-associated protein ATRX. Proc Natl Acad Sci U S A. 104, 11939-11944. (2007)

5. Dhayalan A, Tamas R, Bock I, Tattermusch A, Dimitrova E, Kudithipudi S, Ragozin S, Jeltsch A. The ATRX–ADD domain binds to H3 tail peptides and reads the combined methylation state of K4 and K9. Hum Mol Genet, 20, 2195-2203. (2011)

6. Iwase S, Xiang B, Ghosh S, Ren T, Lewis PW, Cochrane JC, Allis CD, Picketts DJ, Patel DJ, Li H, Shi Y. ATRX ADD domain links an atypical histone methylation recognition mechanism to human mental-retardation syndrome. Nat Struct Mol Biol, 18, 769-776. (2011)

7. Picketts DJ, Higgs DR, Bachoo S, Blake DJ, Quarrell OW, Gibbons RJ. ATRX encodes a novel member of the SNF2 family of proteins: mutations point a common mechanism underlying the ATR-X syndrome. Hum Mol Genet. 5, 1899-1907. (1996)

8. Mitson M, Kelley LA, Sternberg MJ, Higgs DR, Gibbons RJ. Functional significance of mutations in the Snf2 domain of ATRX. Hum Mol Genet. 20, 2603-2610. (2011)

9. Law MJ, Lower KM, Voon HP, Hughes JR, Garrick D, Viprakasit V, Mitson M, De Gobbi M, Marra M, Morris A, Abbott A, Wilder SP, Taylor S, Santos GM, Cross J, Ayyub H, Jones S, Ragoussis J, Rhodes D, Dunham I, Higgs DR, Gibbons RJ. ATR-X syndrome protein targets tandem repeats and influences allele-specific expression in a size-dependent manner. Cell 143, 367-378. (2010)

10. Drané P, Ouararhni K, Depaux A, Shuaib M, Hamiche A. The death-associated protein DAXX is a novel histone chaperone involved in the replication-independent deposition of H3.3. Genes Dev. 24, 1253-1265. (2010)

11. Goldberg AD, Banaszynski LA, Noh KM, Lewis PW, Elsaesser SJ, Stadler S, Dewell S, Law M, Guo X, Li X, Wen D, Chapgier A, DeKelver RC, Miller JC, Lee YL, Boydston EA, Holmes MC, Gregory PD, Greally JM, Rafii S, Yang C, Scambler PJ, Garrick D, Gibbons RJ, Higgs DR, Cristea IM, Urnov FD, Zheng D, Allis CD. Distinct factors control histone variant H3.3 localization at specific genomic regions. Cell. 140, 678-691. (2010)

12. Lewis PW, Elsaesser SJ, Noh KM, Stadler SC, Allis CD. Daxx is an H3.3-specific histone chaperone and cooperates with ATRX in replication-independent chromatin assembly at telomeres. Proc Natl Acad Sci U S A. 107, 14075-14080. (2010)

13. Voon HP, Hughes JR, Rode C, De La Rosa-Velázquez IA, Jenuwein T, Feil R, Higgs DR, Gibbons RJ. ATRX Plays a Key Role in Maintaining Silencing at Interstitial Heterochromatic Loci and Imprinted Genes. Cell Rep. 11, 405-418. (2015)

14. Kernohan KD, Jiang Y, Tremblay DC, Bonvissuto AC, Eubanks JH, Mann MR, Bérubé NG. ATRX partners with cohesin and MeCP2 and contributes to developmental silencing of imprinted genes in the brain. Dev Cell. 18, 191-202. (2010)

15. Kernohan KD, Vernimmen D, Gloor GB, Bérubé NG. Analysis of neonatal brain lacking ATRX or MeCP2 reveals changes in nucleosome density, CTCF binding and chromatin looping. Nucleic Acids Res. 42, 8356-8368. (2014)

16. Levy MA, Kernohan KD, Jiang Y, Bérubé NG. ATRX promotes gene expression by facilitating transcriptional elongation through guanine-rich coding regions. Hum Mol Genet. 24, 1824-1835. (2015)

17. Butler MG. Genomic imprinting disorders in humans: a mini-review. J Assist Reprod Genet. 26, 477-486. (2009)

18. Shioda N, Beppu H, Fukuda T, Li E, Kitajima I, Fukunaga K. Aberrant calcium/calmodulin-dependent protein kinase II (CaMKII) activity is associated with abnormal dendritic spine morphology in the ATRX mutant mouse brain. J Neurosci. 31, 346-358. (2011)

19. Nogami T, Beppu H, Tokoro T, Moriguchi S, Shioda N, Fukunaga K, Ohtsuka T, Ishii Y, Sasahara M, Shimada Y, Nishijo H, Li E, Kitajima I. Reduced expression of the ATRX gene, a chromatin-remodeling factor, causes hippocampal dysfunction in mice. Hippocampus. 21, 678-687. (2011)

20. Howard MT, Malik N, Anderson CB, Voskuil JL, Atkins JF, Gibbons RJ. Attenuation of an amino-terminal premature stop codon mutation in the ATRX gene by an alternative mode of translational initiation. J Med Genet 41, 951-956. (2004)

21. Abidi FE, Cardoso C, Lossi AM, Lowry RB, Depetris D, Mattéi MG, Lubs HA, Stevenson RE, Fontes M, Chudley AE, Schwartz CE. Mutation in the 5′ alternatively spliced region of the XNP/ATR-X gene causes Chudley-Lowry syndrome. Eur J Hum Genet 13, 176-183. (2005)

22. Bergsagel PL, Timblin CR, Kozak CA, Kuehl WM. Sequence and expression of murine cDNAs encoding Xlr3a and Xlr3b, defining a new X-linked lymphocyte-regulated Xlr gene subfamily. Gene. 150, 345-350. (1994)

23. Raefski AS, O'Neill MJ. Identification of a cluster of X-linked imprinted genes in mice. Nat Genet. 37, 620-624. (2005)

24. Davies W, Isles A, Smith R, Karunadasa D, Burrmann D, Humby T, Ojarikre O, Biggin C, Skuse D, Burgoyne P, Wilkinson L. Xlr3b is a new imprinted candidate for X-linked parent-of-origin effects on cognitive function in mice. Nat Genet. 37, 625-629. (2005)

25. Moore LD, Le T, Fan G. DNA methylation and its basic function.

674 Neuropsychopharmacology. 38, 23-38. (2013)
675
676 26. Hutnick LK, Golshani P, Namihira M, Xue Z, Matynia A, Yang XW, Silva AJ,
677 Schweizer FE, Fan G. DNA hypomethylation restricted to the murine forebrain induces
678 cortical degeneration and impairs postnatal neuronal maturation. Hum Mol Genet. 18,
679 2875-2888. (2009)
680
681 27. Feng J, Zhou Y, Campbell SL, Le T, Li E, Sweatt JD, Silva AJ, Fan G. Dnmt1 and
682 Dnmt3a maintain DNA methylation and regulate synaptic function in adult forebrain
683 neurons. Nat Neurosci. 13, 423-430. (2010)
684
685 28. Gibbons RJ, McDowell TL, Raman S, O'Rourke DM, Garrick D, Ayyub H, Higgs
686 DR.Mutations in ATRX, encoding a SWI/SNF-like protein, cause diverse changes in
687 the pattern of DNA methylation. Nat Genet. 24, 368-371. (2000)
688
689 29. Buchan JR, Parker R. Eukaryotic stress granules: the ins and outs of translation. Mol
690 Cell. 36, 932-941. (2009)
691
692 30. Glickman MH, Ciechanover A. The ubiquitin-proteasome proteolytic pathway:
693 destruction for the sake of construction. Physiol Rev. 82, 373-428. (2002)
694
695 31. Martinez-Garay I, Jablonka S, Sutajova M, Steuernagel P, Gal A, Kutsche K. A new
696 gene family (FAM9) of low-copy repeats in Xp22.3 expressed exclusively in testis:
697 implications for recombinations in this region. Genomics. 80, 259-267. (2002)
698
699 32. Hirokawa N, Takemura R. Molecular motors and mechanisms of directional
700 transport in neurons. Nat Rev Neurosci. 6, 201-214. (2005)
701
702 33. Bramham CR, Wells DG. Dendritic mRNA: transport, translation and function. Nat
703 Rev Neurosci. 8, 776-789. (2007)
704
705 34. Rook MS, Lu M, Kosik KS. CaMKIIalpha 3' untranslated region-directed mRNA
706 translocation in living neurons: visualization by GFP linkage. J Neurosci. 20,
707 6385-6393. (2000)
708

709 35. Bliss TV, Collingridge GL. A synaptic model of memory: long-term potentiation in
710 the hippocampus. Nature. 361, 31-39. (1993)
711
712 36. Fukunaga K, Muller D, Miyamoto E. Increased phosphorylation of
713 Ca2+/calmodulin-dependent protein kinase II and its endogenous substrates in the
714 induction of long-term potentiation. J Biol Chem. 270, 6119-6124. (1995)
715
716 37. Scheetz AJ, Nairn AC, Constantine-Paton M. NMDA receptor-mediated control of
717 protein synthesis at developing synapses. Nat Neurosci. 3, 211-216. (2000)
718
719 38. Miller S, Yasuda M, Coats JK, Jones Y, Martone ME, Mayford M. Disruption of
720 dendritic translation of CaMKIIalpha impairs stabilization of synaptic plasticity and
721 memory consolidation. Neuron. 36, 507-519. (2002)
722
723 39. Fukunaga K, Stoppini L, Miyamoto E, Muller D. Long-term potentiation is
724 associated with an increased activity of Ca2+/calmodulin-dependent protein kinase II. J
725 Biol Chem. 268, 7863-7867. (1993)
726
727 40. Ouyang Y, Kantor D, Harris KM, Schuman EM, Kennedy MB. Visualization of the
728 distribution of autophosphorylated calcium/calmodulin-dependent protein kinase II after
729 tetanic stimulation in the CA1 area of the hippocampus. J Neurosci. 17, 5416-5427.
730 (1997)
731
732 41. Balasubramanian S, Hurley LH, Neidle S. Targeting G-quadruplexes in gene
733 promoters: a novel anticancer strategy? Nat Rev Drug Discov. 10, 261-275. (2011)
734
735 42. Peng Q, Warloe T, Berg K, Moan J, Kongshaug M, Giercksky KE, Nesland JM.
736 5-Aminolevulinic acid-based photodynamic therapy. Clinical research and future
737 challenges. Cancer. 79, 2282-2308. (1997)
738
739 43. Qin Y, Hurley LH. Structures, folding patterns, and functions of intramolecular
740 DNA G-quadruplexes found in eukaryotic promoter regions. Biochimie. 90, 1149-1171.
741 (2008)
742
743 44. Bochman ML, Paeschke K, Zakian VA. DNA secondary structures: stability and
744 function of G-quadruplex structures. Nat Rev Genet. 13, 770-780. (2012)

745
746 45. Kikin, O., Zappala, Z., D'Antonio, L. & Bagga, P. S. GRSDB2 and GRS_UTRdb:
747 databases of quadruplex forming G-rich sequences in pre-mRNAs and mRNAs. Nucleic
748 Acids Res 36, D141–D148 (2008)
749
750 46. Gibbons R. Alpha thalassaemia-mental retardation, X linked. Orphanet J Rare Dis. 1,
751 15. (2006)
752
753 47. Villanueva A, Jori G. Pharmacokinetic and tumour-photosensitizing properties of
754 the cationic porphyrin meso-tetra(4N-methylpyridyl)porphine. Cancer Lett. 73, 59-64.
755 (1993)
756
757 48. Dalton JT, Yates CR, Yin D, Straughn A, Marcus SL, Golub AL, Meyer MC.
758 Clinical pharmacokinetics of 5-aminolevulinic acid in healthy volunteers and patients at
759 high risk for recurrent bladder cancer. J Pharmacol Exp Ther. 301, 507-512. (2002)
760
761 49. Perotti C, Casas A, Fukuda H, Sacca P, Batlle A. ALA and ALA hexyl ester
762 induction of porphyrins after their systemic administration to tumour bearing mice. Br J
763 Cancer. 87, 790-795. (2002)
764
765 50. Skalska L, Beltran-Nebot M, Ule J, Jenner RG. Regulatory feedback from nascent
766 RNA to chromatin and transcription. Nat Rev Mol Cell Biol. 18, 331-337. (2017)
767
768 51. Clynes D, Gibbons RJ. ATRX and the replication of structured DNA. Curr Opin
769 Genet Dev. 23, 289-294. (2013)
770
771 52. Li Y, Syed J, Suzuki Y, Asamitsu S, Shioda N, Wada T, Sugiyama H. Effect of
772 ATRX and G-Quadruplex Formation by the VNTR Sequence on α-Globin Gene
773 Expression. Chembiochem. 17, 928-935. (2016)
774
775 53. Roberts DW, Valdés PA, Harris BT, Hartov A, Fan X, Ji S, Leblond F, Tosteson TD,
776 Wilson BC, Paulsen KD. Glioblastoma multiforme treatment with clinical trials for
777 surgical resection (aminolevulinic acid). Neurosurg Clin N Am. 23, 371-377. (2012)
778
779 54. Stummer W, Stocker S, Wagner S, Stepp H, Fritsch C, Goetz C, Goetz AE,
780 Kiefmann R, Reulen HJ: Intraoperative detection of malignant gliomas by

781 5-aminolevulinic acid-induced porphyrin fluorescence. Neurosurgery 42, 518-526.
782 (1998)
783
784 55. Al-Saber F, Aldosari W, Alselaiti M, Khalfan H, Kaladari A, Khan G, Harb G,
785 Rehani R, Kudo S, Koda A, Tanaka T, Nakajima M, Darwish A. The Safety and
786 Tolerability of 5-Aminolevulinic Acid Phosphate with Sodium Ferrous Citrate in
787 Patients with Type 2 Diabetes Mellitus in Bahrain. J Diabetes Res. 8294805. (2016)
788

Figure legends (for main text only)

Figure 1. ATRX regulates *Xlr3b* gene expression. a, Heat map summarizing expression data, and a list of genes exhibiting differential expression between WT and $Atrx^{\Delta E2}$ mouse hippocampus at post-natal day (P) 90 (an FDR < 0.05 and a log2 fold-change of > 0.5). See also **Supplementary Table 1** (a list of genes with an FDR < 0.05 and a log2 fold-change of > 0.5 or < −0.5). n = 7 mice each. **b**, Quantitative real-time RT-PCR showing *Xlr3b* mRNA expression in mouse lysates. $^{**}P < 0.01$ by two-way ANOVA with Bonferroni's post hoc test; n = 8-12 mice at P90. PC, (n=8 each); HP, (n=10 each); HT, (WT, n=10; $Atrx^{\Delta E2}$ n=8); CE, (WT, n=9; $Atrx^{\Delta E2}$, n=10); lung, liver, heart, and kidney, (n=12 each). PC, medial prefrontal cortex; HP, hippocampus; HT, hypothalamus; CE, cerebellum. **c**, (top) Representative immunoblot of P90 mouse brain lysates probed with indicated antibodies. (bottom) Densitometric analysis of Xlr3 normalized to β-tubulin (arbitrary units, A.U.). $^{**}P < 0.01$, $^{*}P < 0.05$ by two-way ANOVA with Bonferroni's post hoc test; n = 4 mice each. **d**, Percentage of 5-methylcytosine (5-mC) as determined by bisulfite sequencing analysis in whole brain from male P90 WT or $Atrx^{\Delta E2}$ mice. $^{**}P < 0.01$ by two-sided unpaired t test. n = 12 clones each. (n = 3 mice each, 4 clones were sequenced per mouse). See also **Supplementary Fig. 2. e**, Xlr3b-ODN showing intramolecular parallel G-quadruplexes, which formed three separate G-quartets stacked 5′ to 3′ with three loops. **f** and **g,** Luciferase activity of Neuro-2a cells co-transfected with plasmids identified in left margin plus other indicated plasmids. Luciferase activity is presented relative to its activity in mock cells. $^{**}P < 0.01$ by one-way ANOVA with Bonferroni's post hoc test; n = 6 biologically independent samples. **h,** (top) Schematic diagram of *Xlr3b*: G-quadruplex-forming sequence (yellow), CGI (gray) and R1 and R2 regions. (bottom) Analysis of R1 and R2 regions in chromatin from hippocampus of $Atrx^{\Delta E2}$ and WT mice by chromatin immunoprecipitation with indicated antibodies. Results are expressed as percent input. $^{**}P < 0.01$, $^{*}P < 0.05$ by two-sided unpaired t test. n = 6 mice at P90. Full-size scans of western blots shown in **Supplementary Fig. 13**.

Figure 2. Xlr3b is found in neuronal RNA granules. a, Pull-down assay and LC-MS/MS analysis of Xlr3-interacting proteins from P60 mouse brain lysates using an Xlr3 antibody. (left) Silver-stained SDS-PAGE gel of protein A sepharose column eluates with rabbit IgG (lane 1) or an Xlr3 antibody (lane 2) in mouse brain lysates. (right) Distribution of identified proteins in a shotgun proteomics experiment. **b**, Immunoblot analysis of GST affinity-column eluates using P60 mouse hippocampal

lysates. Aliquots of extracts (1% input) and eluates were subjected to SDS-PAGE and immunoblotted with indicated antibodies. The experiments were repeated three times with similar results. **c**, Immunoprecipitation (IP) assay with an Xlr3 antibody from P60 mouse hippocampal lysates. Precipitated proteins and inputs were immunoblotted with indicated antibodies. Aliquots of extracts (1% input) and eluates were subjected to SDS-PAGE. The experiments were repeated three times with similar results. **d**, Confocal images showing co-localization of Xlr3 (green) with synaptophysin (red) and MAP2 (blue) in primary mouse cultured neurons at day 21 *in vitro*. Arrowheads indicate synaptophysin-positive puncta. Scale bars: (top) 10μm, (bottom) 5μm. **e**, Confocal images show co-localization of Xlr3 (green) with MAP2 (magenta) in mouse hippocampal CA1. Images at bottom are high-magnification. Scale bars, 10μm. **f**, Confocal images showing co-localization of Xlr3 (magenta) with hnRNP A/B, TIA1, SYTO14 and DCP1a (green) in primary mouse cultured neurons at day 21 *in vitro*. Images at left are enlarged from corresponding boxed areas. Scale bars, 10μm. **g**, (top) Schematic representation of Xlr3b construct. Xlr3b contains a predicted typical nuclear localization signal (NLS) from residues 2-11 and a Cor1/Xlr/Xmr conserved region (Cor1) domain at residues 74-200. (bottom), Confocal images show co-localization of FLAG-tagged Xlr3b constructs (green) with TIA1 (red) in Neuro-2a cells. Nuclear DNA is labeled with DAPI (blue). Scale bars, 10μm. **h**, Neuro-2a cells were transfected with FLAG-tagged Xlr3b constructs, cell lysates were immunoprecipitated (IP) with anti-FLAG antibody, and western blots (WB) were probed with indicated antibodies. To validate an inhibitory effect of XIP, cells were treated 4 h with XIP peptides (1μM). In **d-h**, the experiments were repeated three times with similar results. Full-size scans of western blots shown in **Supplementary Fig. 13**.

Figure 3. Aberrant Xlr3b expression perturbs synaptic plasticity by inhibiting dendritic CaMKIIα mRNA transport. a, Xlr3 interacts with CaMKIIα, Arc and BDNF mRNAs in an RNA immunoprecipitation assay. Total mRNA was precipitated from P90 mouse hippocampal lysates with an Xlr3 antibody. cDNA was analyzed with primers amplifying CaMKIIα, Arc and BDNF mRNAs. $^{**}P < 0.01$ by one-way ANOVA with Bonferroni's post hoc test; n = 5 mice each. **b**, Time-lapse images of mCherry-Xlr3b (red) and GFP-CaMKIIα 3′ UTR (green) co-transported in a dendrite of cultured neuron at day 21 *in vitro*. Granules moved in both anterograde (white arrowhead) and retrograde (yellow arrowhead) directions. Scale bars, 3μm. The experiments were repeated three times with similar results. **c,** (top, right) Representative

kymograph of movement of GFP-CaMKIIα 3′ UTR in a proximal dendrite. Scale bars, 5μm (x-axis) and 5min (y-axis). (top, left) Granules moved in anterograde (white arrowhead) and retrograde (yellow arrowhead) directions. Scale bars, 2μm. See also **Supplementary Video 1**. (bottom) Relative frequency of movement of GFP-CaMKIIα 3′ UTR granules. $^{**}P < 0.01$ by two-way ANOVA with Bonferroni's post hoc test; n = 5 neurons each, a proximal dendrite (20-100μm away from the cell body) per neuron to measure relative frequencies. Cells were treated with XIP (1μM) 4 h before imaging. Imm., immobile; Bidirect., bidirectional movement; Antero., anterograde movement; and Retro., retrograde movement. **d,** The number of GFP-CaMKIIα 3′ UTR (green) and PSD95 (magenta) double-positive puncta. $^{**}P < 0.01$ by one-way ANOVA with Bonferroni's post hoc test; n = 20 neurons each, a proximal dendrite (20-100μm away from the cell body) per neuron. Whiskers represent minima and maxima. **e,** (left) Representative field excitatory post-synaptic potentials (fEPSPs) were recorded from the hippocampal CA1 region of mice. (middle) Changes in fEPSP slope following high frequency stimulation (HFS) recorded in hippocampal CA1. (right) Changes in fEPSP slope following HFS at 1 or 60 min based on analysis shown at left. $^{**}P < 0.01$, $^{*}P < 0.05$ by two-way ANOVA with Bonferroni's post hoc test; WT, $Atrx^{\Delta E2}$, $Atrx^{\Delta E2}$ + XIP, n = 8 mice; $Atrx^{\Delta E2}$ + ANTP, n=6 mice.

Figure 4. 5-ALA represses *Xlr3b* transcription with RNA polymerase II recruitment by modifying G-quadruplex structure. a, 5-ALA metabolism to indicated porphyrins. Succinylacetone inhibits 5-ALA dehydratase (ALAD). PBG, porphobilinogen; PpIX, protoporphyrin IX; FECH, ferrochelatase. **b** and **c,** Luciferase activity in Neuro-2a cells transfected with pGL3-2K or pGL3-2KΔG4 and treated with 5-ALA (0.1, 0.3, 1, 3 or 10μM) **(b)**, or co-administered 10μM 5-ALA and succinylacetone at 1, 10, 100 or 1000μM **(c)** for 48h. Luciferase activity is shown relative to that in vehicle-treated cells. $^{**}P < 0.01$ by one-way ANOVA with Bonferroni's post hoc test; n = 3 biologically independent samples. **d,** Quantitative real-time RT-PCR showing *Xlr3b* mRNA expression in P90 mouse hippocampal lysates. $^{**}P < 0.01$ vs. vehicle-treated WT mice, $^{\#\#}P < 0.01$ vs. vehicle-treated $Atrx^{\Delta E2}$ mice by one-way ANOVA with Bonferroni's post hoc test; n = 6 mice each. **e,** (top) Representative immunoblot of P90 mouse brain lysates probed with indicated antibodies. (bottom) Densitometric analysis of Xlr3 normalized to β-tubulin (arbitrary units, A.U.). $^{**}P < 0.01$ vs. vehicle-treated WT mice, $^{\#\#}P < 0.01$ vs. vehicle-treated $Atrx^{\Delta E2}$ mice by one-way ANOVA with Bonferroni's post hoc test; n = 4 mice each. **f**, Percentage of 5-methylcytosine (5-mC) as determined by bisulfite sequencing analysis

in medial prefrontal cortex (PC) and hippocampus (HP) from male P90 WT or $Atrx^{\Delta E2}$ mice. $^{**}P < 0.01$ by two-way ANOVA with Bonferroni's post hoc test; n = 9 clones. (n = 3 mice. 3 clones were sequenced per mouse.) See also **Supplementary Fig. 10e. g,** (top) The G-quadruplex prediction tool GQRS mapper was used to identify potential G-quadruplex forming sequences in the entire Xlr3b genomic DNA sequence, which is shown with exons highlighted in black and introns highlighted in gray. GQRS mapper provides a G-score (plotted in blue) which indicates the likelihood of G-quadruplex formation. Image is adapted from QGRS mapper (http://bioinformatics.ramapo.edu/QGRS/index.php). (bottom) Analysis of indicated amplicons in chromatin from hippocampus of P90 mice by chromatin immunoprecipitation with indicated antibodies. Results are expressed as percent input. $^{**}P < 0.01$, $^{*}P < 0.05$ vs. vehicle-treated WT mice, $^{\#\#}P < 0.01$, $^{\#}P < 0.05$ vs. vehicle-treated $Atrx^{\Delta E2}$ mice by one-way ANOVA with Bonferroni's post hoc test; n = 6 mice each. Full-size scans of western blots shown in **Supplementary Fig. 13**.

Figure 5. Treatment with 5-ALA counteracts cognitive deficits seen in $Atrx^{\Delta E2}$ mice. **a,** (top) Representative kymograph of movement of GFP-CaMKIIα 3′ UTR in a proximal dendrite. Scale bars, 5μm (x-axis) and 5min (y-axis). (bottom) Relative frequency of movement of GFP-CaMKIIα 3′ UTR granules. Cells were treated with 5-ALA (1μM) for 7 days before imaging. $^{*}P < 0.05$ vs. vehicle-treated WT neurons, $^{\#\#}P < 0.01$ vs. vehicle-treated $Atrx^{\Delta E2}$ neurons by two-way ANOVA with Bonferroni's post hoc test; n = 5 neurons each, a proximal dendrite (20-100μm away from the cell body) per neuron to measure relative frequencies. Imm., immobile; Bidirect., bidirectional movement; Antero., anterograde movement; and Retro., retrograde movement. **b,** The number of GFP-CaMKIIα 3′ UTR (green) and PSD95 (magenta) double-positive puncta in a proximal dendrite. $^{**}P < 0.01$ vs. vehicle-treated WT neurons, $^{\#\#}P < 0.01$ vs. vehicle-treated $Atrx^{\Delta E2}$ neurons by one-way ANOVA with Bonferroni's post hoc test; n = 20 neurons each, a proximal dendrite per neuron. Whiskers represent minima and maxima. **c,** (left) Representative field excitatory post-synaptic potentials (fEPSPs) were recorded from the hippocampal CA1 region of mice. (middle) Changes in fEPSP slope recorded following high frequency stimulation (HFS) were attenuated in $Atrx^{\Delta E2}$ mice, and 5-ALA treatment significantly rescued impaired LTP in hippocampal CA1. (right) fEPSP slope changes following HFS at 1 or 60 min, as shown at left. $^{**}P < 0.01$, $^{*}P < 0.05$ vs. vehicle-treated WT mice, $^{\#\#}P < 0.01$, $^{\#}P < 0.05$ vs. vehicle-treated $Atrx^{\Delta E2}$ mice by two-way ANOVA with post hoc

Bonferroni's multiple comparison test; WT + vehicle, $Atrx^{\Delta E2}$ + vehicle, and $Atrx^{\Delta E2}$ + 5-ALA, n = 8 mice; WT + 5-ALA, n=6 mice. **d-f,** 5-ALA treatment decreased cognitive deficits in $Atrx^{\Delta E2}$ mice based on memory-related tests. Novel-object recognition (NOR) test **(d)**, latency time in retention trials in a passive avoidance (PA) test **(e),** and alternations in a Y-maze test **(f)**. $^{**}P < 0.01$ vs. vehicle-treated WT mice, $^{\#\#}P < 0.01$, $^{\#}P < 0.05$ vs. vehicle-treated $Atrx^{\Delta E2}$ mice by one-way ANOVA with Bonferroni's post hoc test; Respective sample sizes are indicated. **g**, Heat map summarizing expression data (left), and a list of rescued or not-rescued genes (right) between WT, $Atrx^{\Delta E2}$, and 5-ALA treated $Atrx^{\Delta E2}$ mouse hippocampus at post-natal day (P) 90. The list was focused on 31 genes differentially expressed (8 up-regulated and 23 down-regulated) in WT versus $Atrx^{\Delta E2}$ samples **in Supplementary Table 1** (an FDR < 0.05 and a log2 fold-change of > 0.5 or < 0.5). See also **Supplementary Table 3**, which includes 5-ALA treated $Atrx^{\Delta E2}$ group. Rescued or not rescued genes were assessed using the difference between the average value in log2 global normalization. WT, n=7 mice; $Atrx^{\Delta E2}$, n=7 mice; $Atrx^{\Delta E2}$ + 5-ALA, n=4 mice. Full-size scans of western blots shown in **Supplementary Fig. 13**.

On-line Methods

Animals

Male mice (C57BL/6J) were used for all experiments. Mice were housed under climate-controlled conditions with a 12-h light/dark cycle and provided standard food and water ad libitum. Animal studies were conducted in accordance with the Tohoku University institutional guidelines. Ethical approval has been obtained from the Institutional Animal Care and Use Committee of the Tohoku University Environmental and Safety Committee. Generation of homozygous $Atrx^{\Delta E2}$ mice is described in [19]. To generate Thy1-Xlr3b TG mice, Xlr3b cDNA was subcloned into the XhoI site of a mouse Thy1.2 expression cassette (**Supplementary Fig. 9a**). The Thy1 promoter construct was a gift of Joshua Sanes (Addgene plasmid # 20736). The Thy1.2-Xlr3b expression cassette was excised with NotI/PvuI and injected into fertilized eggs of B6 mice at Oriental Bio Service (Kyoto, Japan). Hemizygous Thy1-Xlr3b TG mice were generated by mating founder mice with B6 mice, and offspring were screened by PCR using genomic tail DNA. Primers used for amplification of Xlr3b sequences were ThXl(FW) (5′-GGTATTCATCATGTGCTCCG-3′) and ThXl(RV) (5′-GTTTCTGCCTCTCTTCACAG-3′), and the detected PCR product was 479 bp in founder animals (**Supplementary Fig. 9b**).

Cell culture

Neuro-2a mouse neuroblastoma cells (ATCC, CCL-131, authenticated by the provider using short tandem repeat profiling) were grown in Dulbecco's minimal essential medium (DMEM) supplemented with 10% heat-inactivated fetal bovine serum (FBS) and penicillin/streptomycin (100units/100μg/ml) in a 5% CO_2 incubator at 37°C. Cells were routinely tested for mycoplasma contamination. Transfection was performed using Lipofectamine 2000 (Invitrogen, Carlsbad, CA, USA) transfection reagent according to the manufacturer's protocol. Primary cultures of neurons were established using previously described methods with slight modifications [56]. Briefly, hippocampal tissue was dissected from embryonic day 18 mice and dissociated by trypsin treatment and trituration through a Pasteur pipette. Neurons were plated on coverslips coated with poly-L-lysine in Minimum Essential Medium (Invitrogen) supplemented with 10% FBS, 0.6% glucose (Wako, Osaksa, Japan), and 1mM pyruvate (Sigma-Aldrich, St. Louis, MO, USA). After cell attachment, coverslips were transferred to dishes containing a glial cell monolayer and maintained in Neurobasal medium (Invitrogen) containing 2% B27 supplement (Invitrogen) and 1% GlutaMax (Invitrogen). 5μM Cytosine

β-D-arabinofuranoside (Sigma-Aldrich) was added to cultures at DIV3 after plating to inhibit glial proliferation. Primary neurons were transfected with expression vectors and shRNAs using electroporation (NEPA21; NEPAGENE Co., Ltd. Chiba, Japan) at DIV0.

Plasmid constructs and lentiviral transduction

Plasmids expressing cDNAs encoding Xlr3a, Xlr3b, FAM9A, DNMT1, DNMT3A, H3.3 and DAXX were obtained from Kazusa DNA Research Institute (Promega, Madison, WI, USA) and cDNAs were inserted into pCMV vector. GST-Xlr3b was generated by cloning Xlr3b cDNA into pGEX-4T-1 (Pharmacia Biotech, Piscataway, NJ, USA). ATRX cDNA plasmid (pEGFP-C2-ATRX-HA) was kindly provided by Dr. David Picketts (University of Ottawa, Canada). ATRX shRNA (pSUPER-shATRX1) plasmid was kindly provided by Dr. Nathalie Berube (University of Western Ontario, Canada). GFP-MS2-nls and MS2 binding site (MS2bs)-CaMKIIα 3′UTR constructs were kindly provided by Dr. Kenneth S. Kosik (University of California Santa Barbara Santa Barbara, USA). Xlr3b shRNA was purchased from Sigma-Aldrich (MISSION TRC-Mm2.0 TRCN0000255204). The non-targeting hairpin control SHC002 (Sigma-Aldrich), which containing a sequence that does not target any known human or mouse gene, was used as a negative control (shControl). FLAG-Xlr3b (FL, ΔNLS, Δ74-123, Δ124-200, and Δ158-170) and FLAG-FAM9A (FL and Δ292-304) were generated using the KOD-Plus Mutagenesis kit (Toyobo, Osaka, Japan) according to the manufacturer's protocol. For construction of Xlr3b promoter plasmids, genomic DNA isolated from mouse brain was obtained using a DNeasy Tissue Kit (Qiagen, Valencia, CA, USA). PCR was carried out to amplify a fragment containing the Xlr3b promoter region from nucleotides −2085 to +1 (where +1 is the A of the translation initiation codon). The fragment was then subcloned into the pGL3-basic luciferase reporter (Promega) vector (pGL3-2K) and sequenced. pGL3-2KΔG4 and pGL3-1KΔCGI were generated using the KOD-Plus Mutagenesis kit (Toyobo). The CRISPR-Cas9 and GFP fusion protein expression lentivirus, U6gRNA-Cas9-2A-GFP plus guide Xlr3 sgRNA (Xlr3-Cas9-GFP), was purchased from Sigma-Aldrich. The Xlr3 guide sequence was TCATCTTTCAGTGCCATGG. Lentiviral transduction was performed according to the manufacturer's protocol (Sigma-Aldrich).

Antibodies and peptides

The following primary antibodies were used; anti-Xlr3 (1:500, generated commercially (MBL, Nagoya, Japan) against TDTAGRHSRMDPNLSSDC peptide, anti-ATRX (1:100, Santa Cruz Biotechnology, H300 #sc-15408, Santa. Cruz, CA, USA),

anti-DNMT1 (1:1000, clone 60B1220.1, Abcam #ab13537, Cambridge, UK), anti-DNMT3A (1:1000, clone 64B1446, Abcam #ab13888), anti-β-tubulin (1:5000, clone AC-15, Sigma-Aldrich, #A5441), anti-hnRNP A/B (1:200: Santa Cruz Biotechnology, G-10 #sc-376411), anti-hnRNP A/B (1:200: Santa Cruz Biotechnology, M-15 #sc-82628), anti-DYNC1LI2 (1:1000, clone EPR11230(2), Abcam, #ab178702), anti-DYNLL1 (1:200: Santa Cruz Biotechnology, #sc-136287), anti-histone H3.3 (1:1000, Abcam, #ab62642), anti-DAXX (1:200, Santa Cruz Biotechnology, M-112 #sc-7152), anti-hnRNP D (1:200, clone D6O4F, Cell Signaling Technology, Beverly, MA, USA, #12382), anti-TIA1 (1:200, Santa Cruz Biotechnology, C-20, #sc-1751), anti-FLAG (1:1000, clone M2, Sigma-Aldrich, #F1804), anti-synaptophysin (1:1000, clone SVP-38, Sigma-Aldrich, #S5768), anti-MAP2 (1:10000, Abcam, #ab92434), anti-RNA polymerase II (1:1000, clone CTD4H8, Millipore, MA, USA, #05-623), anti-PSD95 (1:500, clone 6G6-1C9, Abcam, #ab2723), anti-phospho-CaMKII (Thr286/Thr287, 1:5000, [18]) and anti-CaMKIIα/β (1:5000, [18]). For immunoblotting, the following secondary antibodies were used: anti-mouse IgG antibody horseradish peroxidase conjugated (1:5000, Southernbiotech, Birmingham, AL, USA, #1031-05), anti-rabbit IgG antibody horseradish peroxidase conjugated (1:5000, Southernbiotech, #4050-05) and anti-goat IgG antibody horseradish peroxidase conjugated (1:5000, Rockland Immunochemicals Inc., Limerick, PA, USA, #605-4302). For immunocytochemistry and immunohistochemistry, the following secondary antibodies were used: Alexa488-conjugated donkey anti-rabbit (1:500, Invitrogen, #A-21206) Alexa594-conjugated donkey anti-rabbit (1:500, Invitrogen, #A-21207), Alexa 488-conjugated donkey anti-mouse (1:500, Invitrogen, #A-21202), Alexa 594-conjugated donkey anti-mouse (1:500, Invitrogen, #A-21203), Alexa 488-conjugated donkey anti-goat (1:500, Invitrogen, #A-11055), Alexa 594-conjugated donkey anti-goat (1:500, Invitrogen, #A-11058) and DyLight 405-AffiniPure donkey anti-chicken IgY (1:500; Jackson ImmunoResearch, West Grove, PA, USA, #703-475-155). XIP and ANTP control peptides were obtained from the peptide-synthetic service at MBL.

Luciferase assay

Neuro-2a cells were co-transfected with pGL3 plasmids (pGL3-2K, pGL3-2KΔG4 and pGL3-1KΔCGI) plus a pRL-TK plasmid, which contains Renilla luciferase under control of the herpes simplex virus thymidine kinase promoter, with or without other plasmids (ATRX, ATRX shRNA, control shRNA, DNMT1, DNMT3A, H3.3 or DAXX). For *in vitro* DNA methylation assays, pGL3 plasmids were incubated

with 3U CpG methyltransferase (*M.SssI*) (New England Biolabs, Hitchin, UK) for 4h at 37°C in the presence of 1mM S-adenosylmethionine, following the manufacturer's instructions. Firefly and Renilla luciferase activities were measured using the Dual-Luciferase Reporter Assay System (Promega) with a luminometer (Gene Light 55 Luminometer, Microtech, Chiba, Japan). The ratio of Firefly to Renilla luciferase luminescence was calculated.

Identification of Xlr3 interaction proteins by mass spectrometry

Mouse brain tissues at P60 were lysed in buffer containing 50 mM Tris-HCl (pH 7.5), 0.15 M NaCl, 0.1% Triton X-100, 4 mM EDTA, 4 mM EGTA, 1 mM Na_3VO_4, 50 mM NaF, 1 mM DTT, and protease inhibitors (trypsin inhibitor, pepstatin A, and leupeptin), followed by centrifugation at 15,000 × g for 10 min. Supernatants were collected and incubated with Protein A Sepharose column (Protein A HP SpinTrap, GE Healthcare Life Sciences, Piscataway, NJ, USA) with TBS buffer (50 mM Tris-HCl, 0.15 M NaCl, pH 7.5) containing an Xlr3 antibody (10 μg) at 4°C for 4 h with constant rotation. Bound proteins were then washed with TBS and eluted with 2.5% acetic acid. To confirm specific binding, samples were run on SDS-PAGE and the gel was stained using a Silver Stain Kit (Wako). All samples were then analyzed by LC-MS/MS at Oncomics Co., Ltd, (Nagoya, Japan), as a custom service. Proteins identified in control samples pulled down with rabbit IgG (10 μg) were subtracted from identified proteins.

Preparation of proteins binding to GST-Xlr3b

Preparation of proteins was performed using a GST Protein Interaction Pull-Down Kit (Pierce; Thermo Fisher Scientific, Rockford, IL, USA) according to the manufacturer's instructions. GST and GST-Xlr3b were prepared in *E. coli* BL21 and immobilized to glutathione affinity resin. Mouse hippocampal tissues were lysed in buffer containing 50 mM Tris-HCl (pH 7.5), 0.15 M NaCl, 4 mM EDTA, 4 mM EGTA, 1 mM Na_3VO_4, 50 mM NaF, 1 mM DTT, and protease inhibitors (trypsin inhibitor, pepstatin A, and leupeptin), followed by centrifugation and incubation with immobilized glutathione affinity resin containing GST fusion proteins at 4°C for 4 h with constant rotation. Bound proteins were then washed, eluted with glutathione elution buffer, and run on SDS-PAGE.

Immunoprecipitation and immunoblotting

Immunoprecipitation and immunoblotting analysis was performed as described [56]. Briefly, tissues or cells were homogenized in buffer containing 50 mM Tris-HCl, pH

7.5, 0.5% Triton X-100, 0.15 M NaCl, 4 mM EDTA, 4 mM EGTA, 1 mM Na_3VO_4, 50 mM NaF, 1 mM DTT, and protease inhibitors (trypsin inhibitor, pepstatin A, and leupeptin). For immunoprecipitation, lysates were incubated 2 h at 4°C with indicated antibodies with protein A-Sepharose CL-4B (GE Healthcare Life Sciences) in homogenization buffer. Subsequently, immunoprecipitates were washed three times with homogenization buffer, equivalent amounts of protein were electrophoresed on SDS-PAGE and proteins then transferred to an Immobilon polyvinylidene difluoride membrane. After blocking with TTBS solution (50 mM Tris–HCl, pH 7.5, 150 mM NaCl, and 0.1% Tween 20) containing 5% fat-free milk powder for 1 h at room temperature, membranes were incubated overnight at 4 °C with indicated primary antibodies. After washing, membranes were incubated with the appropriate horseradish peroxidase-conjugated secondary antibody diluted in TTBS. Blots were developed using an ECL immunoblotting detection system (Amersham Biosciences, NJ, USA). Immunoreactive bands were visualized using a luminescent image analyzer LAS-4000 (Fuji Film, Tokyo, Japan) and quantified using Image Gauge version 3.41 (Fuji Film).

Subcellular fractionation.

Primary hippocampal neurons at DIV21 were homogenized in ice-cold lysis buffer containing the following (in mM): sucrose 320, HEPES 4, pH 7.4, EGTA 1, and protease inhibitors. The homogenate was centrifuged at 1,000 x g for 10 min at 4°C. The supernatant (S1, postnuclear supernatant) was centrifuged again at 12,000 x g for 15 min to obtain crude synaptosomal fraction (P2). For separating synaptosomal cytosol (LS1) and synaptosomal membrane (LP1), the pellet (P2) was hypo-osmotically lysed (5% lysis buffer; 95% distilled water containing 5% CHAPS and protease inhibitors) for 30 min and centrifuged at 100,000 x g for 60 min. The pellet (LP1) was resuspended in lysis buffer containing 1% Triton X-100 and sonicated.

Immunocytochemistry and immunohistochemistry

Immunocytochemistry and immunohistochemistry were performed as described [56]. Briefly, fixed cells or brain slices with 4% paraformaldehyde in phosphate-buffered saline (PBS) were treated with PBS containing 0.1% Triton X-100 for 10 min. Samples were incubated overnight at 4°C with indicated primary antibodies and then washed in PBS and incubated with appropriate secondary antibodies. Nuclei were stained with 4, 6-diamidino-2-phenylindole (DAPI) (Sigma-Aldrich). To visualize RNA molecules, living neurons were incubated with 50 nM SYTO14 dye (Life Technologies, Carlsbad, CA, USA, #S7576). Fluorescence intensities and images were analyzed by confocal

laser scanning microscopy (LSM700, Carl Zeiss, Thornwood, NY).

Live imaging

Live images of granule movement were captured in dendrites for 15 min (proximal dendrites) or 10 min (distal dendrites) at 15-s intervals in primary neurons at DIV21. Granule movement was analyzed in proximal dendrites (20-100μm) and in distal dendrites (100-200μm) away from the cell body. Relative frequency of movement of GFP-CaMKII 3′ UTR granules was analyzed for a subset of moving granules. Granules that changed direction during the tracking period were defined as bi-directional. Granules were classified as immobile when their movement was < 5 μm during the 15 min (proximal dendrites) or 10 min (distal dendrites) observation period. Kymographs were created using NIH ImageJ software (http://rsb.info.nih.gov/ij/).

RT-PCR and quantitative RT-PCR (RT-qPCR) analysis

Total RNA was purified from P90 mouse brain using an RNeasy Mini Kit (Qiagen) according to the manufacturer's protocol. RNA was reverse-transcribed into single-stranded cDNA using an oligo(dT) primer (Promega) and Moloney murine leukemia virus-reverse transcriptase (Invitrogen), and then subjected to RT-PCR with gene-specific primers. RT-qPCR analysis was performed as described [18] in 48-well plates (Mini Opticon real-time PCR system, Bio-Rad) using iQ SYBR Green Supermix 2× (Bio-Rad). Gene expression was assessed using the differences in normalized Ct (ΔΔCt) method after normalization to GAPDH. Fold-change was calculated by $2^{-\Delta\Delta Ct}$. The following primers were used for RT-PCR and RT-qPCR:
In Fig. 1b, Fig. 4d, supplementary Fig. 1e, supplementary Fig. 9c, and supplementary Fig.10c.
RT-qPCR-Xlr3b(FW) (5′-CAGAAAAAGGAAGGCCACTG-3′)
RT-qPCR-Xlr3b(RV) (5′- GTTTTTCCTTCCTGGCCTGT -3′)
RT-qPCR-GAPDH(FW) (5′-TGTGTCCGTCGTGGATCTGA-3′)
RT-qPCR-GAPDH(RV) (5′-CACCACCTTCTTGATGTCATCATAC-3′)
In supplementary Fig. 1a,
RT-PCR-Xlr3a(FW) (5′-AGCCGAGACCCGACCAAGTGG-3′)
RT-PCR-Xlr3a(RV) (5′-TGTTAGCTGGGTTCTG-3′)
RT-PCR-Xlr3b(FW) (5′-AGCCAAGGCCCGACCAAGTGG-3′)
RT-PCR-Xlr3b(RV) (5′-TAGCTGCTGCGACTGCACCT-3′)

Bisulphite sequencing

Genomic DNA isolated from whole brain, medial prefrontal cortex and hippocampus of WT and Atrx$^{\Delta E2}$ mice at P90 were subjected to bisulphite-mediated C to U conversion using BisulFast (Toyobo, Osaka, Japan) and then used as template for PCR. The PCR products were ligated into the pCR2.1 vector by using a TOPO-TA cloning kit (Invitrogen), according to the manufacturer's instruction. The following primers specific for bisulfite-treated DNA were used for PCR:
Xlr-bisul(FW) (5′-GATTAAGTGGGATGAATTTTTGAGT-3′)
Xlr-bisul(RV) (5′-CCCAAACTAAAAATTTTTCTCATTC-3′)

Chromatin immunoprecipitation (ChIP) assay

Chromatin solutions derived from P90 mouse hippocampus were prepared using the SimpleChIP Plus Enzymatic Chromatin IP Kit (Cell Signaling Technology) and then immunoprecipitated overnight at 4°C using 2 μg indicated antibodies. Assays included normal rabbit IgG as an antibody specificity control. The following antibodies and primers were used:
in Fig. 1
R1(FW) (5′-CCAAGTGGGATGAACCTCTGAGTG-3′)
R1(RV) (5′-CCGCGGAGTCCCACTGTGGAACGT-3′)
R2(FW) (5′-CACAAGTACTATACTAGCTGAAAC-3′)
R2(RV) (5′-GGTTGGTCATACCTATGTAGGAAC-3′)
in Fig. 4
amplicon 1(FW) (5′-CCAAGTGGGATGAACCTCTGAGTG-3′)
amplicon 1(RV) (5′-CCGCGGAGTCCCACTGTGGAACGT-3′)
amplicon 2(FW) (5′-GCCACAGAGGGCAAGGCAAGGGAG-3′)
amplicon 2(RV) (5′-AATGATGTCTTGGTTGGGAATTCCA-3′)
amplicon 3(FW) (5′-AGTATCAGGCTTAGATTTAAAGGA-3′)
amplicon 3(RV) (5′-AAGTCAGGGAGGATGACCAGTCTC-3′)
amplicon 4(FW) (5′-CTGTGCGGGACTCCCATGATACCC-3′)
amplicon 4(RV) (5′-CGTAAGCCCTTCAGCATAAATACT-3′)

RNA immunoprecipitation (RIP) assay

Mouse hippocampal lysates were immunoprecipitated with an Xlr3 antibody (15 μg per sample) followed by RNA isolation using the RiboCluster Profiler RIP-Assay kit (MBL) according to the manufacturer's protocols. Immunoprecipitated RNA was reverse-transcribed into single-stranded cDNA using an oligo(dT) primer (Promega) and

Moloney murine leukemia virus-reverse transcriptase (Invitrogen), and subjected to RT-qPCR with the following gene-specific primers:
BDNF(FW) (5′-TGGCCTAACAGTGTTTGCAG-3′)
BDNF(RV) (5′-GGATTTGAGTGTGGTTCTCC-3′)
CaMKIIα(FW) (5′-GACACCAAAGTGCGCAAACAGG-3′)
CaMKIIα(RV) (5′-GCGAAGCAAGGACGCAGG-3′)
Arc(FW) (5′-AGCAGCAGACCTGACATCCT-3′)
Arc(RV) (5′-GGCTTGTCTTCACCTTCAGC-3′)
GAPDH(FW) (5′-TGTGTCCGTCGTGGATCTGA-3′)
GAPDH(RV) (5′-CACCACCTTCTTGATGTCATCATAC-3′)

Gene microarray analysis

For the oligo-DNA microarray analysis, we used the “3D-Gene” Mouse Oligo chip 24k and Human Oligo chip 25k arrays (Toray Industries Inc, Tokyo, Japan). Total RNA was purified from mouse hippocampus using an RNeasy Mini Kit (Qiagen) according to the manufacturer’s instructions. Total RNA was Cy5-labeled using the Amino Allyl MessageAMP II aRNA Amplification Kit (Applied Biosystems, CA, USA). Labeled aRNA pools were then hybridized 16 h in buffer using the supplier's protocols (www.3d-gene.com). Hybridization signals were scanned using a ScanArray Express Scanner (PerkinElmer) and processed using the GenePixPro version 5.0 software (Molecular Devices).

Electrophysiology

Preparation of hippocampal slices was performed as described [19]. Briefly, brains were rapidly removed from ether-anesthetized mice and chilled in ice-cold oxygenated artificial cerebrospinal fluid (ACSF: 126 mM NaCl, 5 mM KCl, 26 mM $NaHCO_3$, 2.4 mM $CaCl_2$, 1.3 mM $MgSO_4$, 1.26 mM KH_2PO_4, and 10 mM D-glucose). Transverse hippocampal slices (400-μm thickness) were cut using a vibratome (Microslicer DTK-1000, Dosaka EM, Kyoto, Japan) and transferred to a recording chamber where they were allowed to recover at least 1 h at 34°C before recording. ACSF maintained at 34°C was used during the experiment. A concentric bipolar stimulating electrode was placed in the stratum radiatum of CA1 to stimulate the Schaffer collateral pathway. High-frequency stimulation of 100 Hz with 1-s duration was applied twice with a 20-s interval. Traces were digitized with an A/D converter (PowerLab 200; AD Instruments, Castle Hill, Australia) and a computer (Windows, Measurement and Analysis System for LTP: FAL-3000). Paired-pulse responses were measured with inter-stimulus

intervals of 20-500 ms and expressed as the ratio of second stimulated amplitude to the first stimulated amplitude. The hippocampal input/output (I/O) ratio was determined for each group by measuring fEPSP amplitude in response to a series of stimuli with intensities ranging from 0.1 to 1.1 mA. After recording, slices were transferred to a plastic plate on ice to dissect the CA1 region under a microscope. CA1 regions were frozen in liquid nitrogen and stored at -80°C until biochemical analysis.

Drugs

5-ALA (COSMO BIO co., ltd. Tokyo, Japan), and sodium ferrous citrate were kindly provided by SBI Pharmaceuticals Co., Ltd., (Tokyo, Japan). TMPyP4 (5, 10, 15, 20-Tetrakis (1-methyl-4-pyridinio)porphyrin tetra) was purchased from Sigma-Aldrich. For administration to $Atrx^{\Delta E2}$ mice, mice were randomized into 7 groups as follows: 5-ALA (3 and 10 mg/kg, p.o. with sodium ferrous citrate (20:1 mol. ratio) dissolved in distilled water) or vehicle (sodium ferrous citrate dissolved in distilled water) was administered daily from P30 to P90. TMPyP4 (10 and 30 mg/kg, i.p. in saline) or vehicle (saline) was administered twice weekly from P30 to P90. For acute administration, 5-ALA (10 mg/kg, p.o.) was administered 3 h before experiments. Measurement of biodistribution in TMPyP4 and 5-ALA was performed as described in [47, 49].

Behavioral analysis

Adult male mice at P90 were used for behavioral analysis. Animals were subjected to behavioral tests including Y-maze, step-through passive avoidance, novel object recognition and social interaction tasks. All behavioral experiments were conducted with the experimenter blind to mouse genotypes and treatments. In the Y-maze task, spontaneous alternation behavior in a Y-maze was assessed as a task of spatial reference memory. The apparatus consisted of three identical arms (50×16×32 cm^3) of black plexiglas. Mice were placed at the end of one arm and allowed to move freely through the maze during an 8-min session. The sequence of arm entries was manually recorded. An alternation was defined as entries into all three arms on consecutive choices. The maximum number of alternations was defined as the total number of arms entered minus two, and the percentage of alternations was calculated as actual alternations/maximum alternations×100. The total number of arms entered during the session was also determined. In step-through passive avoidance task, training and retention trials of passive avoidance tasks were conducted in a box consisting of dark (25×25×25 cm^3) and light (14×10×25 cm^3) compartments. The floor was constructed

with stainless steel rods, and rods in the dark compartment were connected to an electronic stimulator (Nihon Kohden, Tokyo, Japan). Mice were habituated to the apparatus the day before passive avoidance acquisition. During training, a mouse was placed in the light compartment, and when it entered the dark compartment, the door was closed and an electric shock (0.4 mA for 2 s) was delivered from the floor. The mouse was removed from the apparatus 30 s later. After a 7-day interval, each mouse was placed in the light compartment and step-through latency was recorded over 300 s to assess retention. In the novel object recognition task, mice were individually habituated to an open-field box (35×25×35 cm^3) for 2 consecutive days. During acquisition phase, two objects of the same material were placed symmetrically in the center of the chamber for 10 min. 24 h later, one object was replaced by a novel object, and exploratory behavior was analyzed again for 5 min. After each session, objects were thoroughly cleaned with 70% ethanol to prevent odor recognition. Exploration of an object was defined as rearing on the object or sniffing it at a distance of less than 1 cm, touching it with the nose, or both. Successful recognition was reflected by preferential exploration of the novel object. Discrimination of spatial novelty was assessed by comparing the difference between exploratory contacts of novel and familiar objects and the total number of contacts with both, making it possible to adjust for differences in total exploration contacts. A social interaction test was established using methods described in [57] with slight modifications. WT and $Atrx^{\Delta E2}$ mice were housed in new partitioned cages such that the $Atrx^{\Delta E2}$ mouse occupied one compartment and a weight-matched WT mouse (non-littermate) occupied the other. Forty-eight hours later, the partition was removed and social interaction between mice was videotaped for 10 min. Scored behaviors were divided into four groups. Active social behavior, initiated by the experimental mouse toward the partner, includes: (1) *sniffing* of any part of partner's body including the anogenital area; (2) *following* including direct aggressive attacks accompanied by bites toward the partner's back. Passive social behavior, which occurs as a reaction to active behavior of the partner toward the experimental mouse, includes (3) *receptive responses* when the experimental mouse tolerates sniffing by the partner but shows no defensive or submissive behavior, (4) *escape* in response to a partner's following or aggressive act. Data were analyzed as percentage of time spent in various social behaviors during a 10-min interaction test. The videotapes for all behavioral analysis were scored by a trained observer blind to genotype and treatment.

Actin assays

An *in vitro* F-actin sedimentation assay was performed using the Actin Binding

Protein Spin Down Assay (nonmuscle) kit (BK013; Cytoskeleton, Inc., Denver, CO, USA). Briefly, recombinant Xlr3b protein (1μM) purified from *E. coli* or α-actinin were mixed with polymerized nonmuscle actin (10μM) and incubated 30 min at 22°C. Mixtures were centrifuged to sediment F-actin, and supernatant and pellet fractions were analyzed by SDS–PAGE, followed by Silver staining. Actin polymerization was measured using a pyrene-actin polymerization kit (BK003, Cytoskeleton, Inc.) following the manufacturer's instructions.

CD spectra

All oligonucleotides were purchased from Sigma-Aldrich without further purification. Oligonucleotides for CD spectra were prepared in Li^+ solution or K^+ solution (20 mM lithium cacodylate, pH 7.0, 10 or 100 mM KCl). Annealing was performed by heating to 95°C for 5 min and cooling down slowly to room temperature. CD spectra were measured in 0.5-nm steps from 340 to 220 nm using a JASCO J-805LST Spectrometer and 1-cm quartz cuvettes.

UV melting experiment

UV–Vis melting temperature analyses were performed on a V-650 spectophotometer (JASCO, Japan) with a thermocontrolled PAC-743R cell changer (JASCO, Japan) and a refrigerated and heating circulator F25-ED (Julabo). Oligonucleotides (ODN) (5 μM) in K^+ solution (20 mM lithium cacodylate, pH 7.0, 5 mM KCl) and 1 eq compounds were added. Annealing was performed by heating to 95°C for 5 min and slowly cooling to room temperature. Melting temperature (T_m) of each sample was measured at 295 nm from 15 to 95°C at a rate of 1.0 °C /min. ΔT_m was calculated using T_m values of samples with and without compounds.

Gel electrophoresis

DNA samples (ODN) for gel electrophoresis were prepared similarly to CD spectra samples. Annealing was performed by heating to 95°C for 5 min and cooling slowly to room temperature. Each sample was analysed by native gel (8%) in 1×TBE buffer containing 10 or 100 mM KCl at room temperature. Single-stranded DNA was stained with SYBR® Green I Nucleic Acid Stain (50513, Lonza, Japan). Gels were then imaged by FLA-3000 (FUJIFILM).

DMS footprinting

Samples (ODN) for DMS footprinting were prepared similarly to samples of CD

spectra. DNA samples (10 μL) were then mixed with 1 μL of dimethyl sulfate solution (DMS:ethanol; 4:1, vol/vol). Reactions were quenched with 9 μL stop buffer (3 M -mercaptoethanol:water:NaOAc; 1:6:7, vol/vol). After ethanol precipitation and piperidine cleavage, reactions were separated on 12% denaturing polyacrylamide gels using a Hitachi DNA sequencer. Electrophoresis was conducted under 1.5 kV, ca. 25 mA, and 40°C.

Statistical analysis

To determine the sample size in our experiments, we followed the standard sample sizes used in similar experiments in each of the relevant fields in the literature. All values were expressed as means ± s.e.m. Comparisons between two experimental groups were made using the two-sided unpaired t test. Statistical significance for differences among groups was tested by one-way or two-way ANOVA with post-hoc Bonferroni's multiple comparison test. $P < 0.05$ was considered significant. All the statistical analyses were performed using GraphPad Prism 7 (GraphPad Software, Inc., San Diego, CA, USA). All statistical data were presented in the **Supplementary Table 5**.

Methods-only References

56. Shioda N, Yabuki Y, Wang Y, Uchigashima M, Hikida T, Sasaoka T, Mori H, Watanabe M, Sasahara M, Fukunaga K. Endocytosis following dopamine D2 receptor activation is critical for neuronal activity and dendritic spine formation via Rabex-5/PDGFRβ signaling in striatopallidal medium spiny neurons. Mol Psychiatry. 22,1205-1222. (2017)

57. Spencer CM, Alekseyenko O, Serysheva E, Yuva-Paylor LA, Paylor R. Altered anxiety-related and social behaviors in the Fmr1 knockout mouse model of fragile X syndrome. Genes Brain Behav. 4, 420-430. (2005)

Figure legends (for Supplementary materials only)

Supplementary Fig. 1. **Identification of Xlr3b in mouse brain. a,** Sequence of *Xlr3a/Xlr3b* mRNA and position of PCR primers. **b**, *Xlr3a* and *Xlr3b* primer specificity was confirmed by amplifying respective cDNAs. Serial dilutions of cDNA were prepared and Q-PCR performed. A negative correlation was found between increasing concentrations of cDNA and Ct. The R squared value (coefficient of determination, R^2) was used to determine amplification efficiency. The experiments were repeated twice with similar results. **c,** *Xlr3a* and *Xlr3b* mRNA levels in mouse brain tissue as determined by RT-PCR. Xlr3a (lane 1) and Xlr3b (lane 2) cDNAs served as positive controls. W, wild-type mice; A, $Atrx^{\Delta E2}$ mice; PC, prefrontal cortex; HP, hippocampus; HT, hypothalamus; CE, cerebellum. **d,** Cultured hippocampal neurons were transduced with U6gRNA-Cas9-2A-GFP plus guide Xlr3 sgRNA (Xlr3-Cas9-GFP) lentivirus (top) or control lentivirus expressing GFP (bottom) and immunostained 21 days later. Confocal images revealed loss of Xlr3 (red) immunoreactivity in MAP2-positive (blue) neurons infected with Xlr3-Cas9-GFP but not control GFP virus. In **c** and **d**, the experiments were repeated three times with similar results. **e**, Quantitative real-time RT-PCR showing *Xlr3b* mRNA expression in cells shown in **d**. $^{**}P < 0.01$ by two-sided unpaired t-test. n = 4 biologically independent samples. **f,** Immunoblot (left) and corresponding quantitative (right) analysis of Xlr3 protein in cells shown in **d**. Densitometric analysis of Xlr3 normalized to β-tubulin (arbitrary units, A.U.). $^{**}P < 0.01$ by two-sided unpaired t-test. n = 5 biologically independent samples.

Supplementary Fig. 2. **Bisulfite sequencing evaluation of *Xlr3* CGI methylation in $Atrx^{\Delta E2}$ mouse brain lysates. a,** (top) Schematic showing clusters of Xlr genes on the C57BL/6J X chromosome. See also Raefski and O'Neill, (2005) [23]. (bottom) Location of Xlr3 CpG sites analyzed. Sequences potentially forming G-quadruplex is shaded in gray. **b,** Methylation status of Xlr3 CpG sites. Open circles, unmethylated CpGs; closed circles, methylated CpGs. Male P90 mice were used. n = 3 mice each. 4 independent clones of each sample were sequenced. Roman numerals correspond to those of the CpG sites shown in **a** and **b**.

Supplementary Fig. 3. **G-quadruplex formation by sequences of *Xlr3b* CGI (Xlr3b-ODN). a,** CD spectra of Xlr3b-ODN in Li^+ or K^+ solutions. **b,** Xlr3b-ODN primarily formed intramolecular, parallel G-quadruplexes based on native gel

electrophoresis. **c,** DMS footprinting of G-quadruplexes formed on Xlr3b-ODN in the Li^+ or K^+ solutions. In **a-c**, the experiments were repeated twice with similar results.

Supplementary Fig. 4. **ATRX interacts with DAXX, DNMT1, DNMT3A and H3.3 in mouse hippocampus. a,** Effect of ATRX shRNA in Neuro-2a cells. Immunoblot analysis (left) and densitometric quantification (right) of protein expression. Densitometric analysis of ATRX normalized to β-tubulin (arbitrary units, A.U.). $^{**}P < 0.01$ by two-sided unpaired t-test. n = 3 biologically independent samples. **b**, (left) Representative immunoblot of P90 mouse hippocampal lysates probed with indicated antibodies, (right) Quantitative densitometry analyses. $^{**}P < 0.01$ by two-sided unpaired t-test. n = 6 mice each. **c,** ATRX was immunoprecipitated (IP'd) from P90 WT and $Atrx^{\Delta E2}$ hippocampal extracts, and western blot analysis performed for indicated proteins. Control reactions were performed with IgG. Extracts were assessed as 1% input. The experiments were repeated three times with similar results.

Supplementary Fig. 5. **Purified Xlr3b protein does not bind F-actin or alter actin polymerization. a,** F-actin binding assay. Supernatant (S) and pellet (P) fractions were collected and samples separated on a SDS-gel subsequently stained using a Silver Stain Kit. Reactions were set up as indicated at top. Most α-actinin was found in pellet in the presence of F-actin filaments (lanes 9 and 10), while Xlr3b remained in the supernatant in presence of F-actin filaments (lanes 5 and 6). **b,** Actin polymerization as measured by enhanced fluorescence of pyrene-conjugated actin. Xlr3b addition to purified actin did not alter polymerization. In **a** and **b**, the experiments were repeated twice with similar results.

Supplementary Fig. 6. Xlr3b co-localizes with hnRNP A/B. a-c, Confocal images showing co-localization of FLAG-tagged Xlr3b constructs with hnRNP A/B **(a)**, Dcp1a **(b)** and ubiquitin **(c)** in Neuro-2a cells. Nuclear DNA is labeled with DAPI (blue). Scale bars, 10μm. **d**, Neuro-2a cells were transfected with FLAG-tagged Xlr3b constructs, cell lysates were immunoprecipitated (IP) with anti-FLAG antibody, and western blot (WB) was probed with ubiquitin antibody. **e**, (top) Sequence comparison of Xlr3b residues 158-170 and comparable sequences from the Xlr human orthlogs FAM9A and FAM9B. Identical AAs are in blue and similar in light green. (bottom), Confocal images show localization of FLAG-tagged FAM9A constructs (green) in Neuro-2a cells. Nuclear DNA is labeled with DAPI (blue). Scale bars, 10μm. In **a-e**, the experiments were repeated three times with similar results.

Supplementary Fig. 7. Interaction of Xlr3b AA 158-170 and RBPs. a, Diagram of permeabilization control peptide (antennapedia homeodomain (ANTP)) and Xlr3b inhibitory peptide (XIP). The latter is a 29-AA peptide that contains Xlr3b AA 158-170 plus ANTP. **b,** FL-Xlr3b-transfected cells were treated with XIP (1μM for 4h) and immunostained for TIA1. Scale bars, 20μm. **c,** Pull-down assays with an ANTP antibody assessing TIA1 and hnRNP A/B in P90 mouse brain lysates. Eluted proteins and inputs were immunoblotted with indicated antibodies. Extract samples served as 1% input. IP, immunoprecipitation. In **b** and **c**, the experiments were repeated three times with similar results.

Supplementary Fig. 8. Dynamics of CaMKIIα mRNA transport in distal dendrites. a, Confocal images of mCherry-Xlr3b Δ124-200 or Δ158-170 (red) and GFP-CaMKIIα 3′ UTR (green) in cultured neurons at day 21 *in vitro*. Scale bars, 10μm. The experiments were repeated three times with similar results. **b,** (top, left) A confocal image of GFP-CaMKIIα 3′ UTR in primary mouse cultured neurons at day 21 *in vitro*. Scale bar, 50μm. Images at right is enlarged from corresponding boxed area. Scale bar, 10μm. See also **Supplementary Video 2**. (bottom) Relative frequency of movement of GFP-CaMKIIα 3′ UTR granules. $^{**}P < 0.01$ by two-way ANOVA with Bonferroni's post hoc test; n = 5 neurons each, a distal dendrite (100-200μm away from the cell body) per neuron to measure relative frequencies. Cells were treated with XIP (1μM) 4 h before imaging. Imm., immobile; Bidirect., bidirectional movement; Antero., anterograde movement; and Retro., retrograde movement.

Supplementary Fig. 9. Generation of Thy1-Xlr3b transgenic mice. a, Genomic organization of Thy1 gene (top) and the transgenic construct (bottom). The Xlr3b cDNA was subcloned into a XhoI site of the Thy1.2 expression cassette. Blue boxes, untranslated exons. **b,** Representative PCR genotyping using tail DNA of transgenic founders (#13 and #57). M, size marker. **c**, Quantitative real-time RT-PCR showing *Xlr3b* mRNA expression in P90 mouse hippocampal lysates. $^{**}P < 0.01$ by one-way ANOVA with Bonferroni's post hoc test; n = 6 mice each. TG, Xlr3b transgenic mouse. **d**, (top) Representative immunoblot of mouse hippocampal lysates probed with Xlr3 and β-tubulin antibodies, (bottom) Densitometric analysis of Xlr3 normalized to β-tubulin (arbitrary units, A.U.). $^{**}P < 0.01$ by two-sided unpaired t-test; n = 5 mice each. **e,** Effect of Xlr3b shRNA in cultured neurons. Immunoblot analysis (top) and densitometric quantification (bottom) of protein expression. Densitometric analysis of

Xlr3 normalized to β-tubulin (arbitrary units, A.U.). *P < 0.05 by two-sided unpaired t-test; n = 3 biologically independent samples. **f,** (left) Method for isolation of synaptosomal membrane fractions from cultured neurons. The procedure for the subcellular fractionation is described in Methods. P1, nucleus/cell debris; S1, postnuclear supernatant; S2, cytosol fraction; P2, crude synaptosomal fraction; LS1, synaptosomal cytosol fraction; LP1, synaptosomal membrane fraction. Immunoblot showing CaMKIIα and postsynaptic marker, PSD95 between S2, LS1, and LP1 in cultured neurons from WT mice. (middle and right) Immunoblot and corresponding quantitative analysis of CaMKIIα and PSD95 proteins at LP1 and whole cell lysates in cultured neurons. Densitometric analyses of CaMKIIα normalized to PSD95 (arbitrary units, A.U.). **P < 0.01 by one-way ANOVA with Bonferroni's post hoc test. (In WT vs. Xlr3b-TG, **P < 0.01 by two-sided unpaired t-test.) LP1, n = 5 biologically independent samples; whole cell lysates, n = 4 biologically independent samples. **g,** (top) Representative field excitatory post-synaptic potentials (fEPSPs) were recorded from the hippocampal CA1 region of mice. (left), Changes in fEPSP slope following high frequency stimulation (HFS) were attenuated in Xlr3b-TG mice in hippocampal CA1. (right), Changes in fEPSP slope following HFS at 1 or 60 min. **P < 0.01 by two-way ANOVA with Bonferroni's post hoc test; n = 8 mice each. **h**, Paired pulse facilitation (left) and input-output relationship (right) were recorded. n = 5 mice each. There were no significant changes between the groups. **i**, LTP-induced CaMKIIα phosphorylation in the hippocampus. (left) Representative images of immunoblots using antibodies against phosphorylated CaMKIIα (pCaMKIIα) and total CaMKIIα. (right) Densitometric analysis of pCaMKIIα normalized to total CaMKIIα (arbitrary units, A.U.). **P < 0.01, *P < 0.05, vs. WT mice before high-frequency stimulation (HFS), ##P < 0.01, #P < 0.05, before HFS vs. after HFS in each group by two-way ANOVA with Bonferroni's post hoc test. Respective sample sizes are indicated. **j-l,** Xlr3b-TG mice show memory deficits. Novel-object recognition (NOR) test **(j)**, Latency time in retention trials in a passive avoidance (PA) test **(k),** Alternations in a Y-maze test **(l)** are shown. **P < 0.01, *P < 0.05 by two-sided unpaired t-test. Respective sample sizes are indicated.

Supplementary Fig. 10. TMPyP4 treatment inhibits Xlr3b expression. a, The binding effect of Protoporphyrin IX (PpIX), hemin and TMPyP4 on G-quadruplexes formed by Xlr3b-ODN based on a UV melting experiment. **b,** Luciferase activity of Neuro-2a cells transfected with pGL3-2K or pGL3-2KΔG4 and treated with TMPyP4 (1, 3, 10, 30 and 100μM) for 48 h. Luciferase activity is shown relative to activity in

vehicle-treated cells. $^{**}P < 0.01$ by one-way ANOVA with Bonferroni's post hoc test; n = 3 biological replicates. **c,** Quantitative real-time RT-PCR showing *Xlr3b* mRNA expression in mouse hippocampal lysates. $^{**}P < 0.01$ vs. vehicle-treated WT mice, $^{\#\#}P < 0.01$ vs. vehicle-treated $Atrx^{\Delta E2}$ mice by one-way ANOVA with Bonferroni's post hoc test; n = 4 mice each. **d**, (top) Representative immunoblot of mouse hippocampal lysates probed with Xlr3 and β-tubulin antibodies, (bottom) Densitometric analysis of Xlr3 normalized to β-tubulin (arbitrary units, A.U.). $^{**}P < 0.01$ vs. vehicle-treated WT mice, $^{\#\#}P < 0.01$ vs. vehicle-treated $Atrx^{\Delta E2}$ mice by one-way ANOVA with Bonferroni's post hoc test; n = 4 mice each. **e**, Methylation status of Xlr3b CpG sites. Open circles, unmethylated CpGs; closed circles, methylated CpGs. Male P90 mice were used. n = 3 mice each. three independent clones of each sample were sequenced.

Supplementary Fig. 11. TMPyP4 treatment rescues cognitive deficits seen in $Atrx^{\Delta E2}$ mice. a, Relative frequency of movement of GFP-CaMKIIα 3′ UTR granules in distal dendrites. Cells were treated with 5-ALA (1μM) for 7 days before imaging. $^{**}P < 0.01$, $^{*}P < 0.05$ vs. vehicle-treated WT neurons, $^{\#\#}P < 0.01$ vs. vehicle-treated $Atrx^{\Delta E2}$ neurons by two-way ANOVA with Bonferroni's post hoc test; n = 5 neurons each, a distal dendrite (100-200μm away from the cell body) per neuron to measure relative frequencies. Imm., immobile; Bidirect., bidirectional movement; Antero., anterograde movement; and Retro., retrograde movement. **b**, Paired pulse facilitation (left) and input-output relationship (right) were recorded. n = 5 mice each. There were no significant changes between the groups. **c**, (left) Immunoblot and corresponding quantitative analyses of CaMKIIα and PSD95 proteins at LP1 (synaptosomal membrane fractions) and whole cell lysates in cultured neurons. Densitometric analyses of CaMKIIα normalized to PSD95 (arbitrary units, A.U.). $^{*}P < 0.05$ vs. vehicle-treated WT neurons, $^{\#}P < 0.05$ vs. vehicle-treated $Atrx^{\Delta E2}$ neurons by one-way ANOVA with Bonferroni's post hoc test; n = 5 biologically independent samples. (right) LTP-induced CaMKIIα phosphorylation in the hippocampus. Representative images of immunoblots using antibodies against phosphorylated CaMKIIα (pCaMKIIα) and CaMKIIα. Densitometric analysis of pCaMKIIα normalized to total CaMKIIα (arbitrary units, A.U.). $^{*}P < 0.05$, vs. WT mice before high-frequency stimulation (HFS), $^{\#\#}P < 0.01$, before HFS vs. after HFS in each group by two-way ANOVA with Bonferroni's post hoc test; n = 4 mice each. **d-f,** TMPyP4 treatment rescued cognitive deficits in $Atrx^{\Delta E2}$ mice based on memory-related behavioral tests. Novel-object recognition (NOR) test **(d)**, latency time in retention trials in a passive avoidance (PA) test **(e),** alternations in a Y-maze test **(f)** are shown. $^{**}P < 0.01$ vs. vehicle-treated WT mice, $^{\#}P < 0.05$, $^{\#\#}P <$

0.01 vs. vehicle-treated Atrx$^{\Delta E2}$ mice by one-way ANOVA with Bonferroni's post hoc test; Respective sample sizes are indicated. **g,** Atrx$^{\Delta E2}$ mice show withdrawal in social interactions with WT mice. Atrx$^{\Delta E2}$ mice showed enhanced passivity, higher escape duration and decreased social activity, such as following and sniffing behaviors, in social interactions with WT mice. These behaviors are dramatically improved by 5-ALA treatment. $^{**}P < 0.01$, $^{*}P < 0.05$ vs. vehicle-treated WT mice, $\#\# P < 0.01$, $\#P < 0.05$ vs. vehicle-treated Atrx$^{\Delta E2}$ mice by one-way ANOVA with Bonferroni's post hoc test; Respective sample sizes are indicated. **h**, Measurements of TMPyP4 fluorescence levels. Chronic intraperitoneal injection of TMPyP4 in P90 mice increased fluorescence levels in some tissues, including brain. Respective sample sizes are indicated. **i,** Measurements of body weight following chronic TMPyP4 administration on day 60 (i.p. twice weekly from P30 to P90). Respective sample sizes are indicated. **j,** Measurements of 5-ALA levels in P90 mouse brain after oral administration (3mg/kg, p.o.). Respective sample sizes are indicated.

Supplementary Fig. 12. Schematic showing outcomes following *Atrx* mutation. ATRX binds to parallel G-quadruplexes in *Xlr3b* CGIs along with DNMTs, DAXX and H3.3, regulating *Xlr3b* gene expression through DNA methylation in cooperation with DMNTs. CaMKIIα mRNA locates in neuronal dendrites, and its transport is dynamically regulated by the motor protein, dynein. CaMKIIα translation enhances synaptic efficacy postsynaptically, which is critical for learning and memory. In control neurons, ATRX binds G-quadruplex-forming DNA in *Xlr3b* CGIs, inhibiting *Xlr3b* expression through DNA methylation. In *Atrx* mutant neurons, aberrant expression of Xlr3b protein occurs through DNA de-methylation at the site. Xlr3b protein has RNA binding capacity and cooperates with RNA binding proteins (RBPs), and inhibits dendritic transport of CaMKIIα mRNA, resulting synaptic dysfunction. Treatment with G-quadruplex (G4) ligand 5-ALA represses *Xlr3b* transcription, antagonizing both synaptic dysfunction and cognitive deficits in *Atrx* mutant mice.

Supplementary Fig. 13. Full-size scans of western blots shown in figures.

Supplementary Table 1. List of genes exhibiting differential expression in hippocampus of P90 WT and Atrx$^{\Delta E2}$ mice.

Supplementary Table 2. Xlr3 interaction partners identified in proteomic screen using LC-MS/MS analysis.

Supplementary Table 3. List of genes exhibiting differential expression in P90 WT, Atrx$^{\Delta E2}$ and 5-ALA treated Atrx$^{\Delta E2}$ mouse hippocampus.

Supplementary Table 4. List of genes exhibiting differential expression in P90 WT, Atrx$^{\Delta E2}$ and TMPyP4 treated Atrx$^{\Delta E2}$ mouse hippocampus.

Supplementary Table 5. Summary of all statistical data.

Supplementary Video 1. Time-lapse imaging of GFP-MS2-labeled CaMKIIα mRNA (GFP-CaMKIIα 3′ UTR) in a proximal dendrite of a cultured WT neuron.

Supplementary Video 2. Time-lapse imaging of GFP-MS2-labeled CaMKIIα mRNA (GFP-CaMKIIα 3′ UTR) in a distal dendrite of a cultured WT neuron.

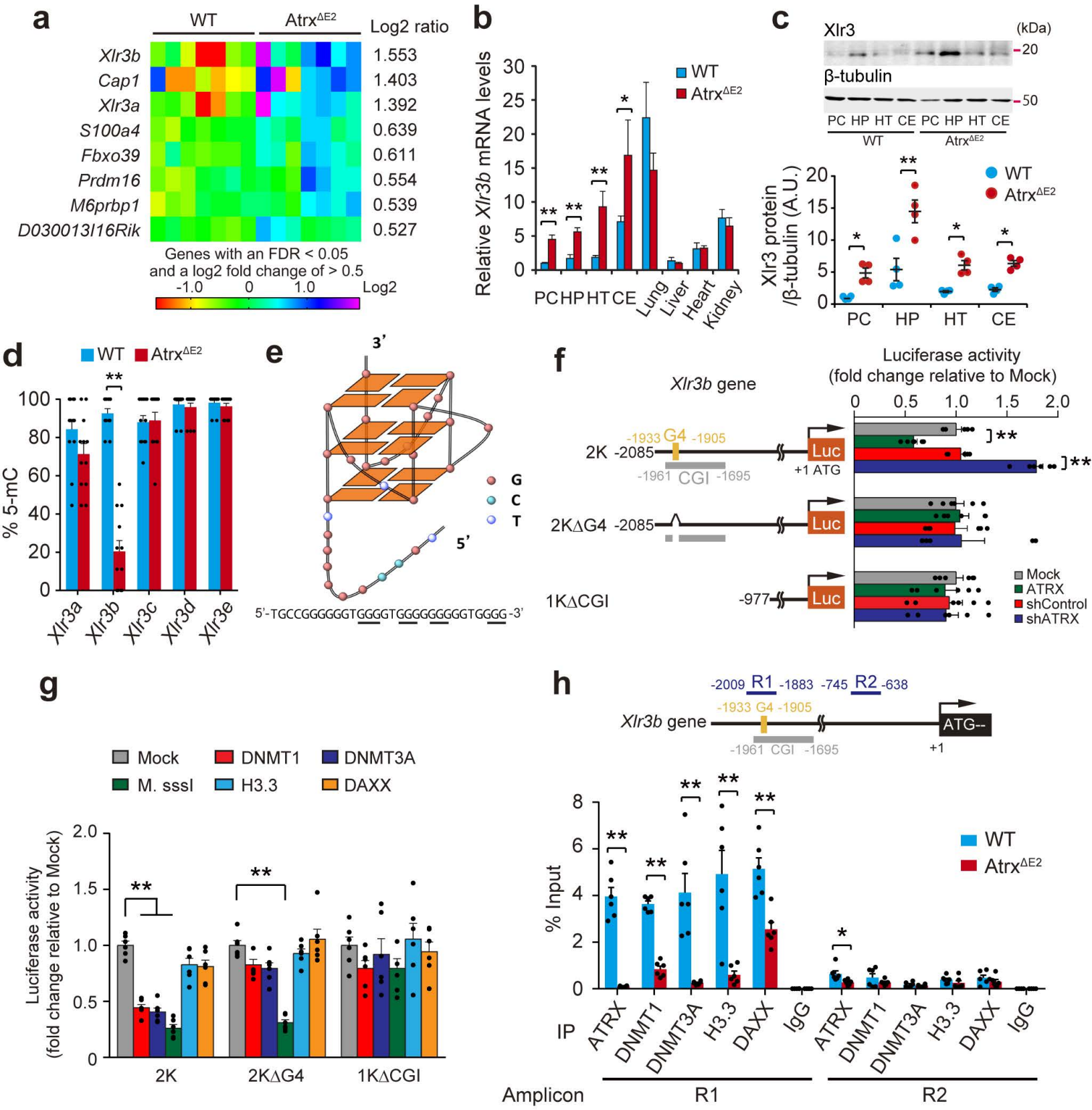

Fig. 1

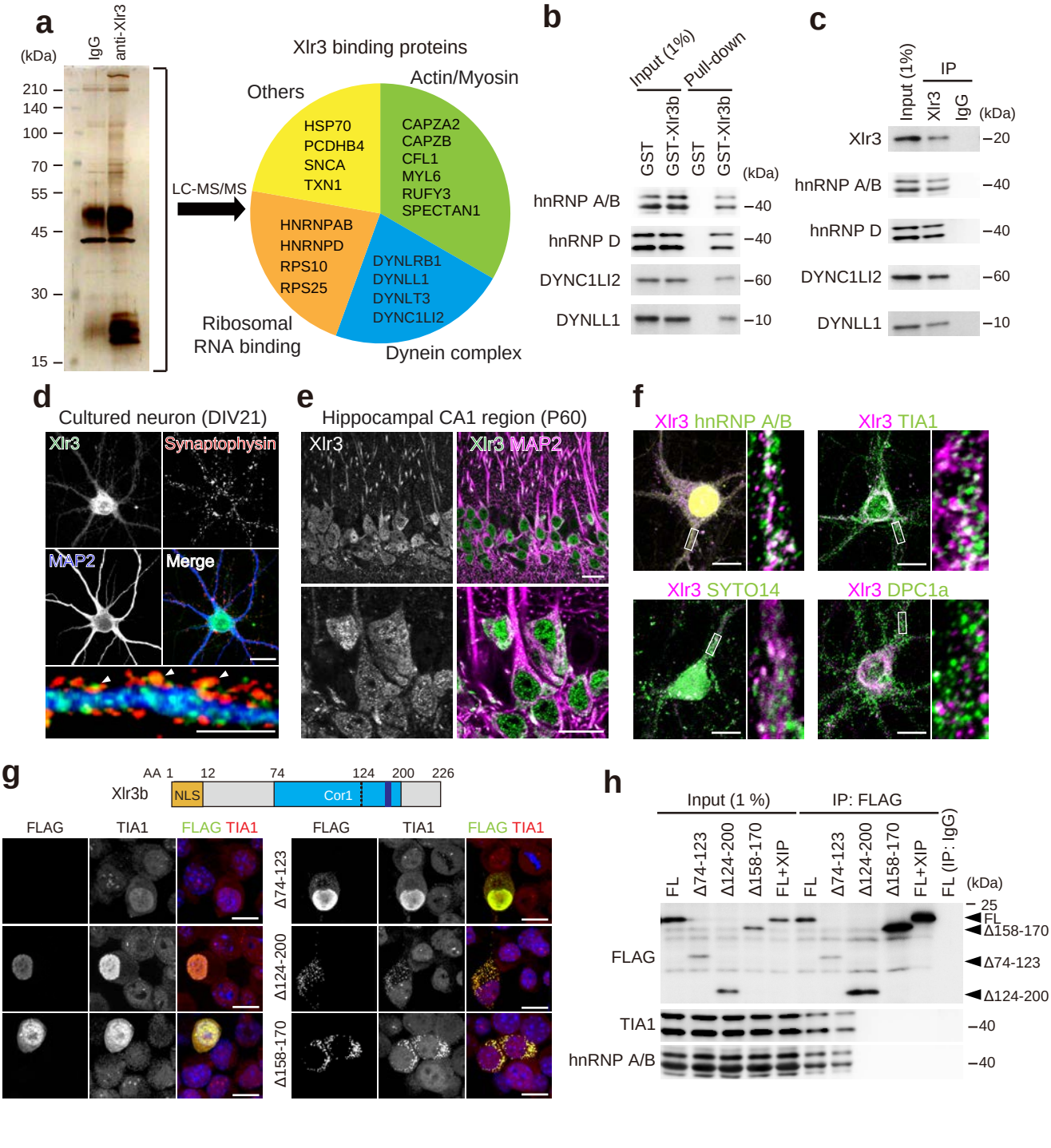

Fig. 2

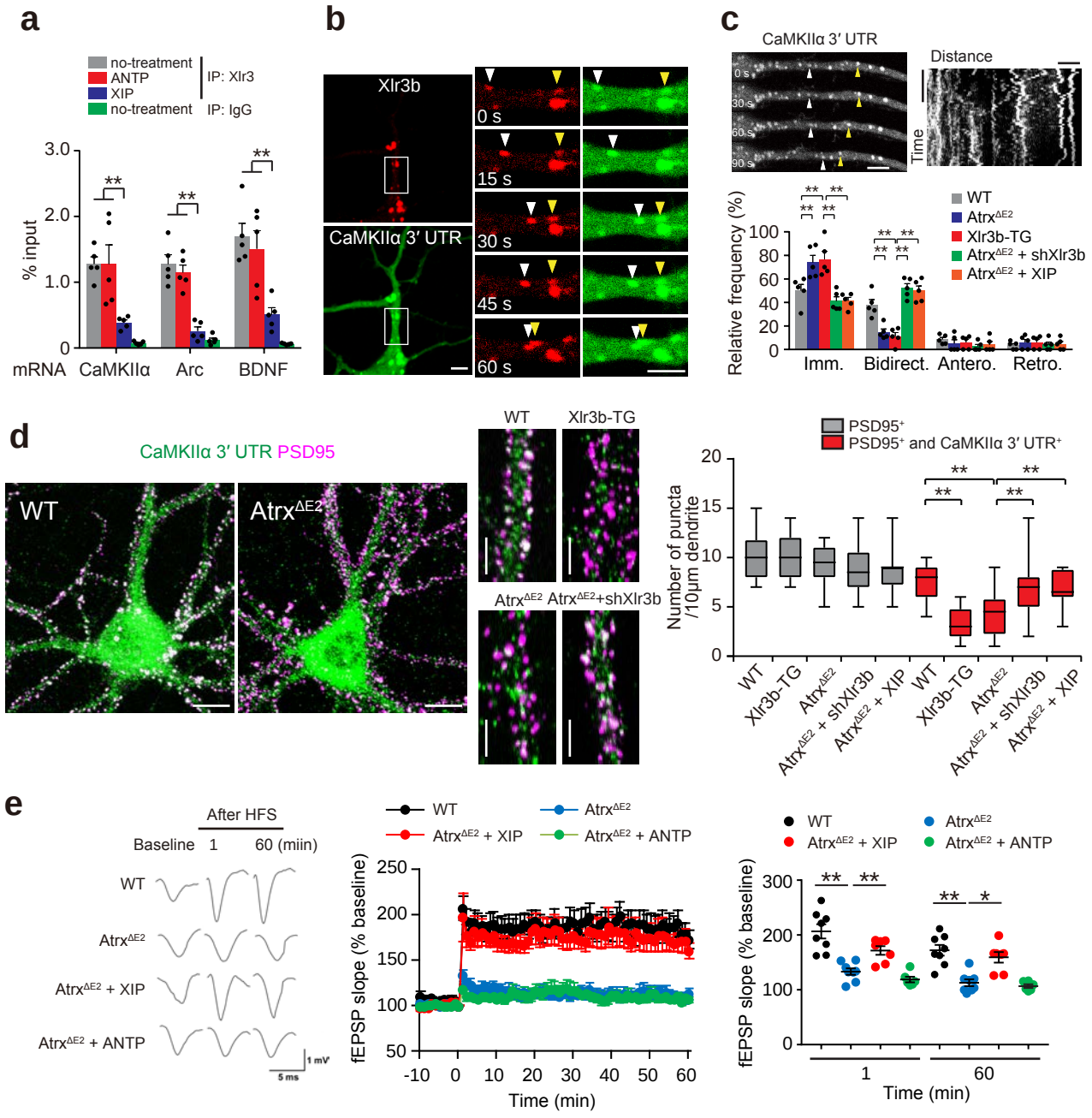

Fig. 3

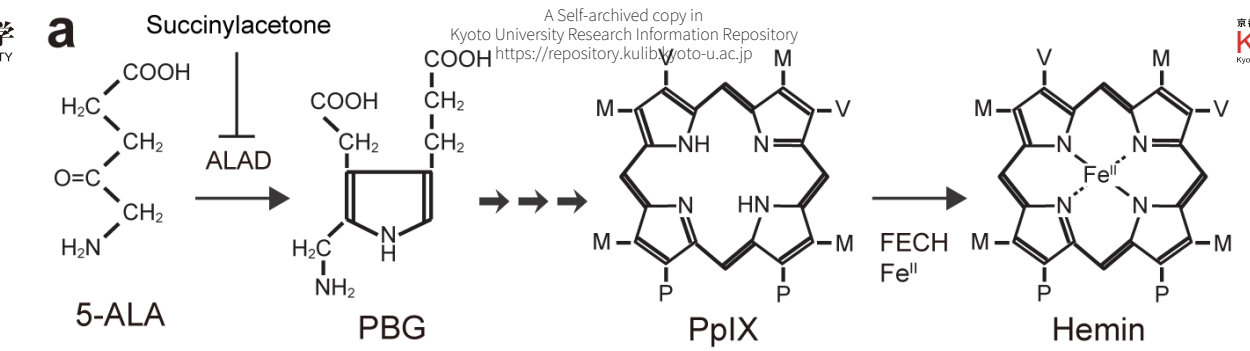

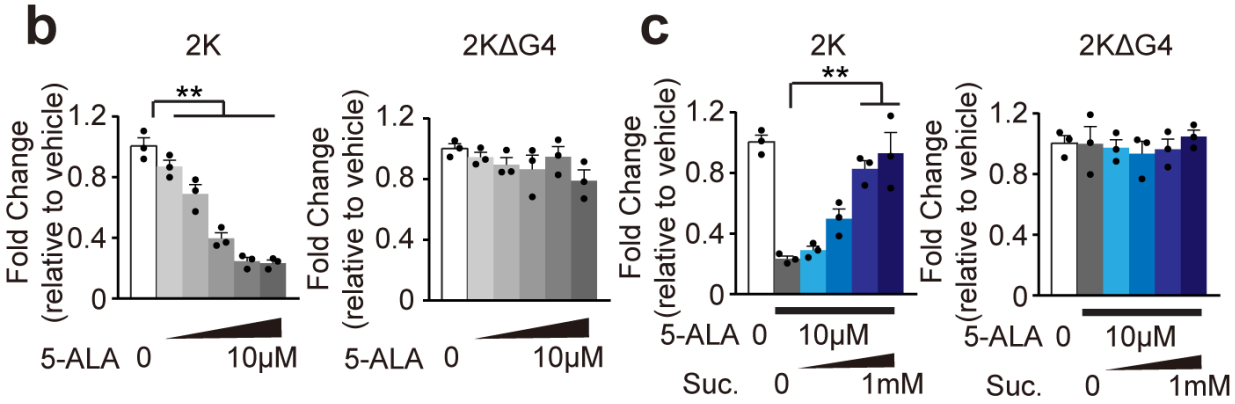

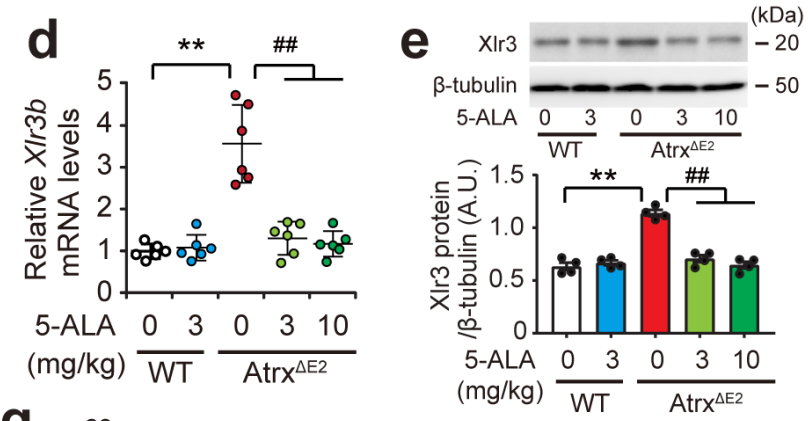

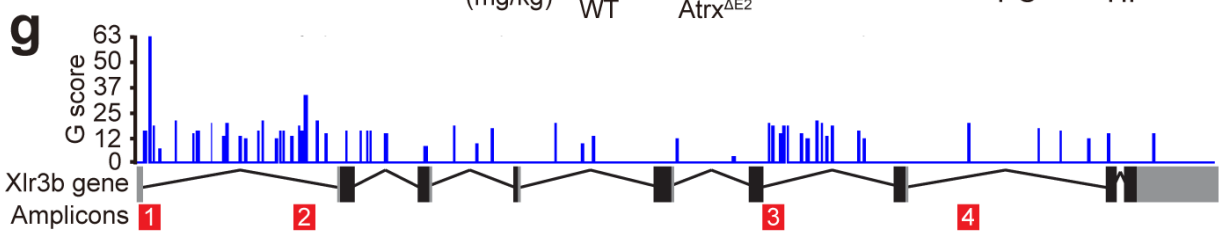

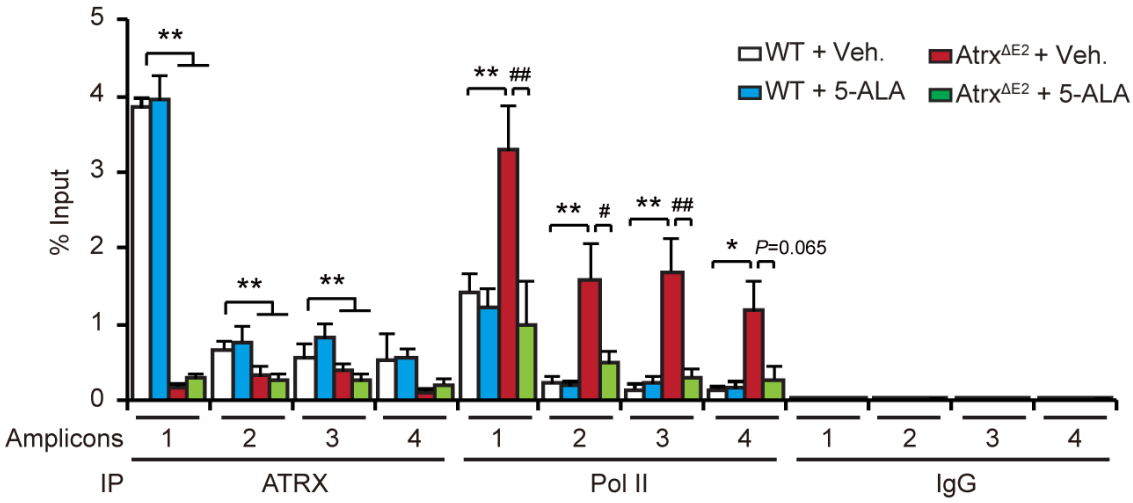

Fig. 4

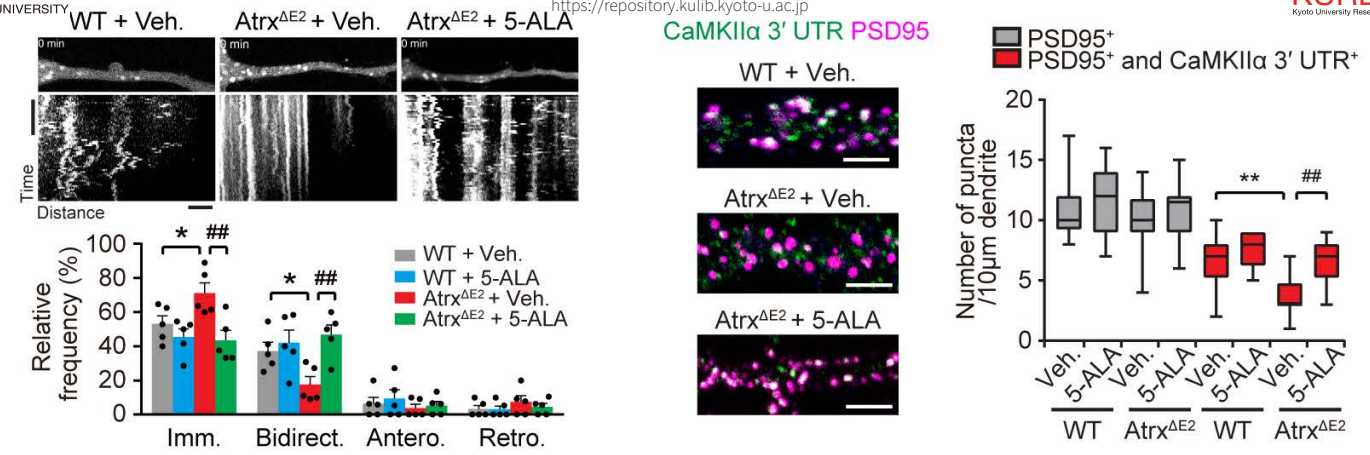

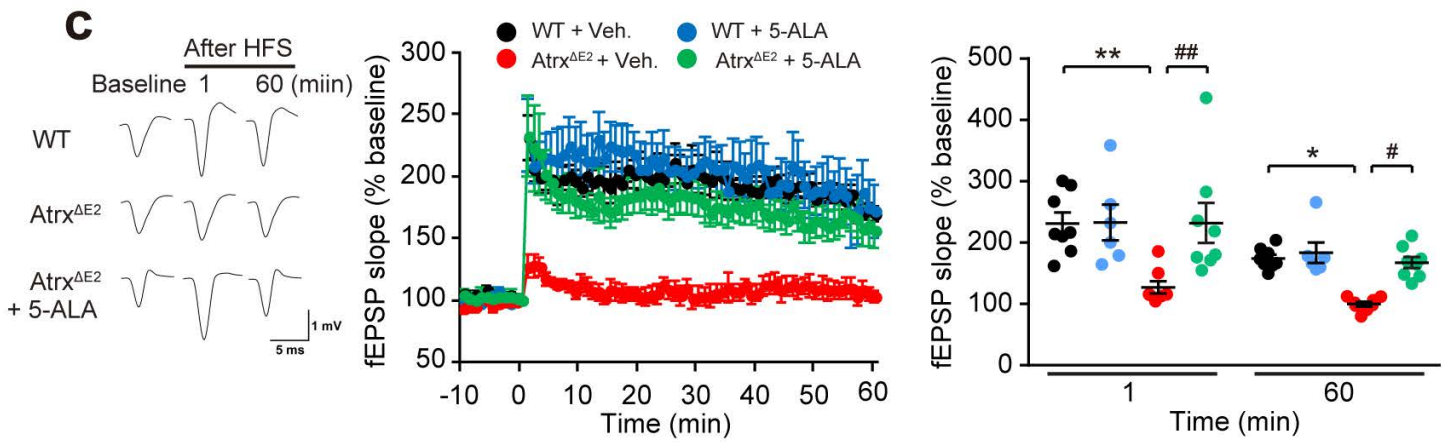

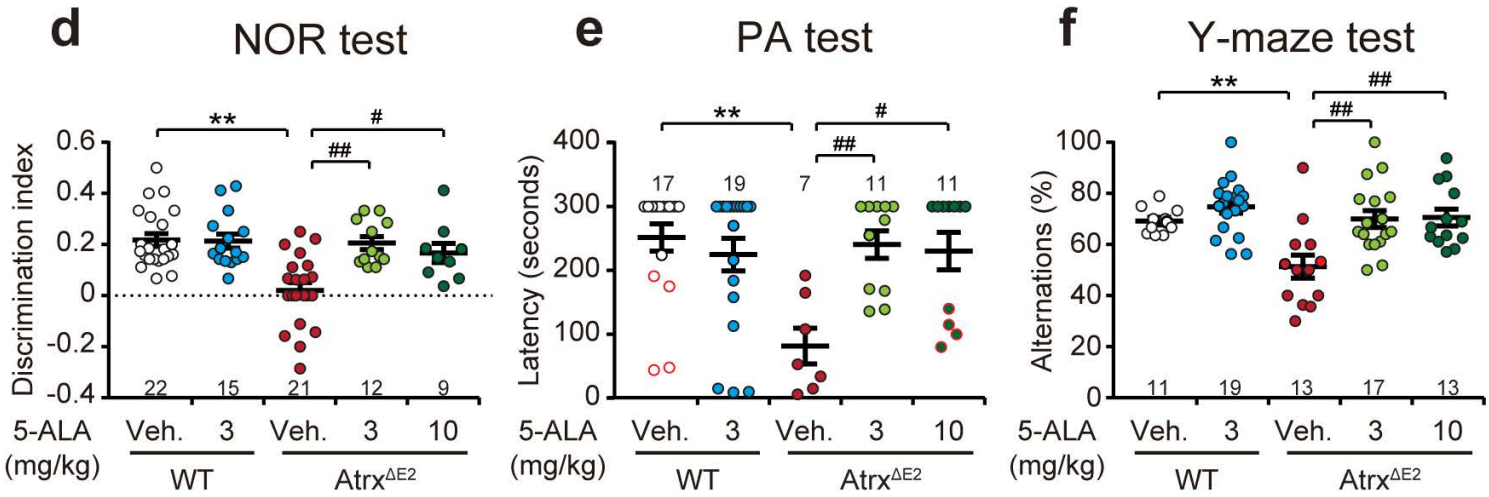

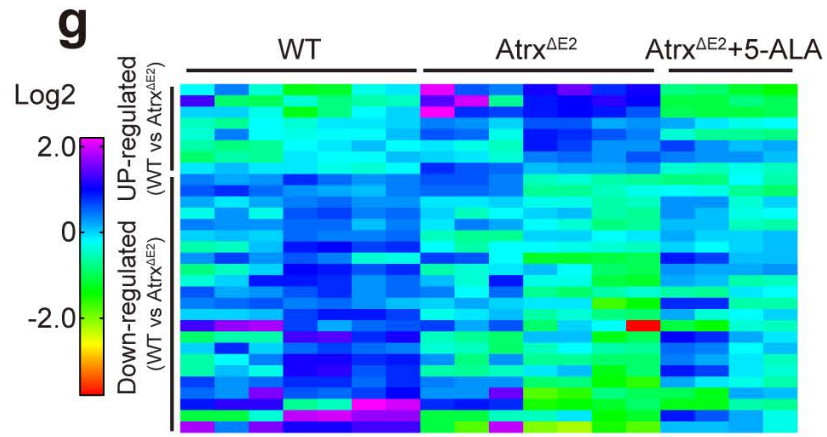

WT vs Atrx$^{\Delta E2}$		Atrx$^{\Delta E2}$ vs Atrx$^{\Delta E2}$+5-ALA	
Up	8 genes	Not Rescued	*Prdm16, M6prbp1*
		Rescued	*Xlr3b, Cap1, Xlr3a, S100a4 Fbxo39, D030013I16Rik*
Down	23 genes	Rescued	*Plcb4, F2r, Atp7a, Zic1, ENSMUSG00000056615, Inpp4b, Vash2, Arsj, Tmie, Rgs16, Agxt2l1, Zic2, Mrvi1, Ramp3, Slc17a6, Spry2*
		Not Rescued	*Rora, Cpne9, 4921511K06Rik, Klhdc8a, Atrx, Cbln1, Tac2*

Fig. 5